Study of phase-field lattice Boltzmann models based on the conservative Allen-Cahn equation

Amirhosein Begmohammadi,[1] Reza Haghani-Hassan-Abadi,[2] Abbas Fakhari,[3] and Diogo Bolster[1]
[1]*Department of Civil and Environmental Engineering and Earth Sciences, University of Notre Dame, Indiana 46556, USA*
[2]*School of Mechanical Engineering, College of Engineering, University of Tehran, Tehran, Iran*
[3]*ANSYS Inc., Lebanon, New Hampshire 03766, USA*

(Received 3 September 2019; revised 18 June 2020; accepted 13 July 2020; published 12 August 2020)

Conservative phase-field (CPF) equations based on the Allen-Cahn model for interface tracking in multiphase flows have become more popular in recent years, especially in the lattice-Boltzmann (LB) community. This is largely due to their simplicity and improved efficiency and accuracy over their Cahn-Hilliard–based counterparts. Additionally, the improved locality of the resulting LB equation (LBE) for the CPF models makes them more ideal candidates for LB simulation of multiphase flows on nonuniform grids, particularly within an adaptive-mesh refinement framework and massively parallel implementation. In this regard, some modifications—intended as improvements—have been made to the original CPF-LBE proposed by Geier *et al.* [Phys. Rev. E **91**, 063309 (2015)] which require further examination. The goal of the present study is to conduct a comparative investigation into the differences between the original CPF model proposed by Geier *et al.* [Phys. Rev. E **91**, 063309 (2015)] and the so-called improvements proposed by Ren *et al.* [Phys. Rev. E **94**, 023311 (2016)] and Wang *et al.* [Phys. Rev. E **94**, 033304 (2016)]. Using the Chapman-Enskog analysis, we provide a detailed derivation of the governing equations in each model and then examine the efficacy of the above-mentioned models for some benchmark problems. Several test cases have been designed to study different configurations ranging from basic yet informative flows to more complex flow fields, and the results are compared with finite-difference simulations. Furthermore, as a development of the previously proposed CPF-LBE model, axisymmetric formulations for the proposed model by Geier *et al.* [Phys. Rev. E **91**, 063309 (2015)] are derived and presented. Finally, two benchmark problems are designed to compare the proposed axisymmetric model with the analytical solution and previous work. We find that the accuracy of the model for interface tracking is roughly similar for different models at high viscosity ratios, high density ratios, and relatively high Reynolds numbers, while the original CFP-LBE without the additional time-dependent terms outperforms the so-called improved models in terms of efficiency, particularly on distributed parallel machines.

DOI: 10.1103/PhysRevE.102.023305

I. INTRODUCTION

Multiphase flows occur in many industrial and environmental settings. Examples include cavitation, flow through porous media, bubble columns, boiling heat transfer, and bubble reactors in micro devices. One common technique for modeling two-phase flows is interface tracking, which can broadly be classified in one of two categories: sharp-interface [1,2] and diffuse-interface [3,4] methods. Sharp-interface methods aim to replicate the true tiny scale of interfaces in multiphase flows but might face numerical challenges and instabilities when dealing with rapid topological changes at the interface due to discontinuous properties of fluids. On the other hand, diffuse-interface models make a compromise by defining an interface width in such a way to make fluid properties vary smoothly across the interface, typically over a larger scale than occurs in reality, however, with the added benefit that they do not suffer numerical instability problems to the same extent as their sharp-interface counterparts. This smooth interfacial thickness provides many advantages when trying to model large deformations of the interface in multiphase flows. The dynamics of the finite interface can often be modeled with a nonlinear advection-diffusion equation to describe the evolution of the phase field; common implementations include the Cahn-Hilliard (C-H) [5] or Allen-Cahn (A-C) [6] models. A variety of different numerical approaches can be taken to solve these equations. Here we focus on the lattice-Boltzmann method (LBM).

Over the past few decades, phase-field LB models have attracted a great deal of attention, demonstrating high accuracy and efficiency. Phase-field LB models based on the C-H equation (CHE) are abundant in the literature (e.g., Refs. [7–10]); however, restrictions on density and viscosity ratios that can be simulated can be significant for some of these models.

In the CHE, the evolution of the concentration consists of two stages: First, there is a fast phase separation, and in the second stage a phase coarsening occurs. The total mass of the system is conserved [11]. Despite these advantages, the CHE includes the need to calculate fourth-order spatial derivatives which present numerical challenges, potentially compromising one of the LB's main advantages of locality, which typically enables highly scalable parallel computing. Meanwhile, the second-order A-C equation (ACE) [6] is better suited to local computations in the LB framework. A shortcoming of the ACE was that in its original form it is not conservative. However, since then, it has been modified for use as a phase-field model [12] and reformulated in conservative form [13]. Geier

et al. [14] were the first to propose a phase-field LB model based on the conservative A-C equation (CACE) and show its mass conservation properties. As part of their approach, one must calculate the normal to the interface which requires the gradient of the phase field. Geier *et al.* [14] presented two different formulations based on finite differences and central moments. The central moment approach takes advantage of the locality of the collision operator in the LB model, which is appealing for massive parallel implementation. However, the finite-difference version, which does not preserve locality, was shown to be more accurate in several benchmark problems. Later, Ren *et al.* [15] proposed a multiple-relaxation-time (MRT) LB model based on the CACE. They argued that the Geier *et al.* [14] LB model does not recover the CACE in complete detail. To rectify this, they modified the equilibrium distribution function and added additional source terms to the model to recover the CACE more accurately. These source terms include a temporal derivative of the phase field, whose calculation is again not ideal for parallel implementation. At the same time, Wang *et al.* [16] published a similar idea based on the Bhatnagar-Gross-Krook (BGK) collision model and presented a comparative study between the A-C– and C-H–based LB models. Comparing the two aforementioned models [15,16], it can be seen that the former [15] is the MRT version of the latter [16]. Hereafter, we refer to the original model proposed by Geier *et al.* as model A [14] and refer to the BGK version of the model proposed by Ren *et al.* [15] as model B [16]. Recently, Liang *et al.* [17] proposed a phase-field LB model, based on the modified CFP-LBE. Wang *et al.* [18] also presented a brief overview of the recent progress in phase-field LB modeling and its applications. Both of these works claimed, without any numerical investigation, that the model proposed by Geier *et al.* [14] is inaccurate due to the emergence of artificial terms in the recovered interface-tracking equation (i.e., not the desired CACE). As part of this work we will delve deeper into such findings and show that the effect of these additional terms is practically negligible.

To date, most existing multiphase LB models are based on the Cartesian coordinate system, although numerous practical problems exist for which axisymmetry is perhaps more natural [19–25]. In these problems, instead of using fully three-dimensional (3D) LB models, 2D axisymmetric formulations can be effective, making computations much more efficient. However, adapting LB methods from the Cartesian frame to the axisymmetric frame requires the addition of source terms to the governing equations, the structure of which are not *a priori* clear. Many axisymmetric LB models have been proposed, mostly for single-phase flows [26]. The first axisymmetric multiphase model was presented by Premnath and Abraham [27], where they added appropriate source terms into the He *et al.* [28] model in the Cartesian coordinate to account for the axisymmetric contribution of inertia, viscosity, and surface tension. Huang *et al.* [22] proposed an improved axisymmetric LB model and used this model to simulate bubble rising. The aforementioned models, however, are limited to low density ratios. Mukherjee and Abraham [29] introduced source terms associated with density and velocity gradients to present an axisymmetric model that was stable at higher density ratios at the expense of a more complicated discretization stencil [8]. Recently, Liang *et al.* [30] presented an axisymmetric multiphase LB model based on the CHE that was quite different from previous ones, in that none of the additional source terms required calculation of additional gradients, making it simpler and more consistent to implement. Moreover, the axisymmetric CHE and Navier-Stokes (N-S) equations can be precisely derived from their model. This model is able to handle moderate density ratios; however, it remains unstable at high ones. Liang *et al.* [31] proposed an axisymmetric multiphase model based on the CACE which can handle high density ratios, departing from the Cartesian model of Ren *et al.* [15].

In this paper, an investigation of two phase-field LB models is performed to compare the accuracy of the Geier [14] model (model A) and the Ren [15] and Wang [16] models (model B) for interface tracking. In particular, we perform Chapman-Enskog analysis to recover the ACE as related to each LB model, clearly demonstrating the differences between them. We design a series of numerical experiments to study the effect of the distinct terms for different benchmark problems. Doing so, we explain why the effect of the additional terms is negligible via a theoretical analysis. In the final section, a new axisymmetric model based on the ACE is proposed that is able to handle high density and viscosity ratios.

II. CARTESIAN EQUATIONS

The CACE governing the transport of phase field $\phi(\boldsymbol{x}, t)$ is given by [13]

$$\frac{\partial \phi}{\partial t} + \nabla \cdot (\phi \boldsymbol{u}) = \nabla \cdot [M(\nabla \phi - \lambda \boldsymbol{n})], \tag{1}$$

with

$$\lambda = \frac{1 - 4(\phi - \phi_0)^2}{W}, \tag{2}$$

where t is the time, $\boldsymbol{u}$ is velocity, M is mobility, W is the interfacial width, $\phi_0 = (\phi_h + \phi_l)/2$ indicating the location of the interface, and $\boldsymbol{n} = \frac{\nabla \phi}{|\nabla \phi|}$ is the unit vector normal to the interface. The subscripts l and h stand for the light and heavy phases, respectively.

The continuity and momentum equations for incompressible multiphase flows can be written as

$$\nabla \cdot \boldsymbol{u} = 0, \tag{3}$$

$$\rho\left(\frac{\partial \boldsymbol{u}}{\partial t} + \boldsymbol{u} \cdot \nabla \boldsymbol{u}\right) = -\nabla p + \nabla \cdot \{\mu[\nabla \boldsymbol{u} + (\nabla \boldsymbol{u})^T]\} + \boldsymbol{F}_s + \boldsymbol{F}_b, \tag{4}$$

where $\boldsymbol{F}_s$ and $\boldsymbol{F}_b$ are surface tension and body forces, respectively; p is the hydrodynamic pressure; and μ is the dynamic viscosity. In this study, the surface tension force is given by [32]

$$\boldsymbol{F}_s = \mu_\phi \nabla \phi, \tag{5}$$

where $\mu_\phi = 4\beta(\phi - \phi_l)(\phi - \phi_h)(\phi - \phi_0) - \kappa \nabla^2 \phi$ is the chemical potential for binary fluids. $\beta = 12\sigma/W$ and $\kappa = 3\sigma W/2$ are coefficients related to surface tension and interface thickness.

In the following we will present LB model A (Sec. II A) and LB model B (Sec. II B) to recover Eq. (1). It should

be noted that in order to compare the interface tracking equations, both in the Cartesian and axisymmetric systems, the hydrodynamic LBE used in this paper is the same as that used in model B. In all cases we use finite differences to calculate the normal to the interface, and for simplicity only the BGK collision operator is considered.

A. LB model A

The LBE proposed by Geier *et al.* [14] for interface tracking based on the CACE is

$$h_i(\boldsymbol{x}+\boldsymbol{c}_i\delta t, t+\delta t) - h_i(\boldsymbol{x}, t) = -\frac{h_i(\boldsymbol{x}, t) - h_{i,A}^{\mathrm{eq}}(\boldsymbol{x}, t)}{\tau} + \left(1 - \frac{1}{2\tau}\right)\delta t F_{i,A}(\boldsymbol{x}, t), \tag{6}$$

with the source term

$$R_{i,A}(\boldsymbol{x}, t) = \delta t \lambda w_i \boldsymbol{c}_i \cdot \boldsymbol{n}, \tag{7}$$

where h_i is the phase-field distribution function in the ith direction, τ is the phase-field relaxation time, w_i is the weight coefficient, and $\boldsymbol{c}_i$ is the mesoscopic velocity set. For the D2Q9 lattice used in this work $w_0 = 4/9$, $w_{1-4} = 1/9$, $w_{5-8} = 1/36$, and the mesoscopic velocity set is [33]

$$\boldsymbol{c}_i = c\begin{cases}(0,0), & i=0\\ (\cos\theta_i, \sin\theta_i), & \theta_i = (i-1)\pi/2, \quad i=1-4,\\ (\cos\theta_i, \sin\theta_i)\sqrt{2}, & \theta_i = (2i-9)\pi/4, \quad i=5-8\end{cases} \tag{8}$$

where $c = \delta x/\delta t$ and δx and δt are the length scale and time length scale of the underlying lattice, respectively. The equilibrium distribution function for model A $h_{i,A}^{\mathrm{eq}}$ is defined as

$$h_{i,A}^{\mathrm{eq}} = w_i\phi\left[1 + \frac{\boldsymbol{c}_i\cdot\boldsymbol{u}}{c_s^2} + \frac{(\boldsymbol{c}_i\cdot\boldsymbol{u})^2}{2c_s^4} - \frac{\boldsymbol{u}\cdot\boldsymbol{u}}{2c_s^2}\right], \tag{9}$$

where $c_s = c/\sqrt{3}$ for this system, the mobility is defined as

$$M = c_s^2\left(\tau - \frac{1}{2}\right)\delta t, \tag{10}$$

and the phase field is computed by taking the zeroth moment of the distribution function

$$\phi = \sum_i h_i. \tag{11}$$

Using the computed phase field, the density of the fluid is calculated by linear interpolation as

$$\rho = \rho_l + \frac{\phi - \phi_l}{\phi_h - \phi_l}(\rho_h - \rho_l). \tag{12}$$

Using the Chapman-Enskog expansion, Appendix A, we can recover the continuum level equation associated with this LB model. Details of this expansion are provided in Refs. [15,16]. The outcome of the expansion yields the following continuum level equation for the evolution of the phase field:

$$\frac{\partial\phi}{\partial t} + \nabla\cdot(\phi\boldsymbol{u}) = \nabla\cdot[M(\nabla\phi - \lambda\boldsymbol{n})] + \frac{M}{c_s^2}\nabla\cdot\left[\frac{\partial(\phi\boldsymbol{u})}{\partial t} + \nabla(\phi\boldsymbol{u}\boldsymbol{u})\right]. \tag{13}$$

By comparing the recovered equation (13) with the CACE (1), it can be seen that the additional terms appearing in the recovered equation are

$$\frac{M}{c_s^2}\nabla\cdot\left[\frac{\partial(\phi\boldsymbol{u})}{\partial t} + \nabla(\phi\boldsymbol{u}\boldsymbol{u})\right]. \tag{14}$$

B. LB model B

The following LB equation was proposed by Wang *et al.* [16] to recover the CACE:

$$h_i(\boldsymbol{x}+\boldsymbol{c}_i\delta t, t+\delta t) - h_i(\boldsymbol{x}, t) = -\frac{h_i(\boldsymbol{x}, t) - h_{i,B}^{\mathrm{eq}}(\boldsymbol{x}, t)}{\tau} + \left(1 - \frac{1}{2\tau}\right)R_{i,B}(\boldsymbol{x}, t). \tag{15}$$

where the source term is defined by

$$R_{i,B}(\boldsymbol{x}, t) = \frac{\delta t\, w_i}{c_s^2}\boldsymbol{c}_i\cdot\left[c_s^2\lambda\boldsymbol{n} + \frac{\partial(\phi\boldsymbol{u})}{\partial t}\right], \tag{16}$$

The local equilibrium distribution function h_i^{eq} for this model can be defined as

$$h_{i,B}^{\mathrm{eq}} = w_i\phi\left[1 + \frac{\boldsymbol{c}_i\cdot\boldsymbol{u}}{c_s^2}\right]. \tag{17}$$

The mobility and phase field are derived the same as before. For this model we can also perform the Chapman-Enskog expansion to recover the CACE given by Eq. (1).

C. Model A and model B differences

Comparing models A and B, two primary differences stand out:

(1) Comparing Eq. (7) and Eq. (16), model B has an additional time-dependent source term, $\frac{\partial(\phi\boldsymbol{u})}{\partial t}$. This removes the time-dependent term from Eq. (13) that emerges in the asymptotic expansion of model A.

(2) Looking at Eq. (9) and Eq. (17), the local equilibrium distribution functions h_i^{eq} are different for these models, where model A has quadratic terms in velocity, while model B does not. Removing the quadratic terms eliminates the $\nabla(\phi\boldsymbol{u}\boldsymbol{u})$ from Eq. (13) in model A.

In this paper, we aim to understand the effects of these additional terms in the CACE. Model A, by not having a time-dependent term in the LB equation, provides a platform to reduce computational costs and memory requirements in high-performance computing, and previous studies have demonstrated the success and promise of model A [34–36]. However, these additional terms that arise from the expansion are troubling and present a potential problem that must be better understood. In our investigation on the effects of these two terms, we use the hydrodynamic equations proposed in Ref. [17].

III. AXISYMMETRIC EQUATIONS

Here the theory for isothermal multiphase flow in axisymmetric systems is presented. By transforming $(x, y, z) \rightarrow (r, \theta, z)$, where r, z, θ denote the radial, axial, and azimuthal directions, respectively, one can write the CACE (1) for an axisymmetric coordinate system. Assuming flow does not have any swirl motion and azimuthal velocity is zero; the axisymmetric conservative A-C equation (ACACE) can then be written as [31]

$$\partial_t \phi + \partial_\alpha(\phi u_\alpha) + \frac{\phi u_r}{r} = \partial_\alpha[M(\partial_\alpha(\phi) - \lambda n_\alpha)] + \frac{M}{r}[\partial_r \phi - \lambda n_r] \tag{18}$$

or in the following simpler form [31]:

$$\partial_t(r\phi) + \partial_\alpha(r\phi u_\alpha + M\phi\delta_{\alpha r}) = \partial_\alpha[M(\partial_\alpha(r\phi) - r\lambda n_\alpha)], \tag{19}$$

where $\alpha = [r, z]$.

The continuity and momentum equations in the axisymmetric coordinate system can be expressed as [31,37]

$$\partial_\alpha(u_\alpha) = -\frac{u_r}{r}, \tag{20}$$

$$\partial_t(\rho u_\alpha) + \partial_\beta(\rho u_\beta u_\alpha) = -\partial_\alpha(p) + \partial_\beta[\rho\nu(\partial_\beta u_\alpha + \partial_\alpha u_\beta)] + \tilde{F}_{s\alpha} + F_{b\alpha} + F_{\mathrm{axi},\alpha}, \tag{21}$$

with

$$F_{\mathrm{axi},\alpha} = \frac{\nu\rho(\partial_r u_\alpha + \partial_\alpha u_r)}{r} - \frac{2\rho\nu u_r \delta_{\alpha r}}{r^2} - \frac{\rho u_r u_\alpha}{r}, \tag{22}$$

where $\tilde{F}_{s\alpha}$ is the modified surface tension force given by $\tilde{F}_{s\alpha} = (\mu - \kappa\frac{\partial_r\phi}{r})\partial_\alpha\phi$.

LB model for interface tracking

Here we propose the equivalent axisymmetric model associated with LB model A. The LBE can be written as

$$h_i(\boldsymbol{x} + \boldsymbol{c}_i\delta t, t + \delta t) - h_i(\boldsymbol{x}, t) = -\frac{h_i(\boldsymbol{x}, t) - h_{i,A}^{\mathrm{eq}}(\boldsymbol{x}, t)}{\tau} + \left(1 - \frac{1}{2\tau}\right)\delta t F_{i,A}(\boldsymbol{x}, t), \tag{23}$$

with the forcing term given by

$$F_{i,A}(\boldsymbol{x}, t) = w_i r c_{i\alpha}[n_\alpha \lambda]. \tag{24}$$

The equilibrium distribution function is defined as

$$h_{i,A}^{\mathrm{eq}} = \Gamma_{i,A}\phi + w_i\frac{c_{i\alpha}M\delta_{\alpha r}}{c_s^2},$$
$$\Gamma_{i,A} = r w_i\left[1 + \frac{c_{i\alpha}u_\alpha}{c_s^2} + \frac{(c_{i\alpha}u_\alpha)^2}{2c_s^4} - \frac{u_\alpha u_\alpha}{2c_s^2}\right]. \tag{25}$$

The following LB model is proposed by Liang *et al.* [31] which is the axisymmetric extension of their Cartesian model [16] and is known as model B in this article:

$$h_i(\boldsymbol{x} + \boldsymbol{c}_i\delta t, t + \delta t) - h_i(\boldsymbol{x}, t) = -\frac{h_i(\boldsymbol{x}, t) - h_{i,B}^{\mathrm{eq}}(\boldsymbol{x}, t)}{\tau} + \left(1 - \frac{1}{2\tau}\right)\delta t F_{i,B}(\boldsymbol{x}, t), \tag{26}$$

with forcing term

$$F_{i,B}(\boldsymbol{x}, t) = w_i r\frac{c_{i\alpha}[\partial_t(\phi u_\alpha + M\phi\delta_{\alpha r}/r) + c_s^2 n_\alpha\lambda]}{c_s^2}, \tag{27}$$

and equilibrium distribution function

$$h_{i,B}^{\mathrm{eq}} = \Gamma_{i,B}\phi + w_i\frac{c_{i\alpha}M\delta_{\alpha r}}{c_s^2}, \qquad \Gamma_{i,B} = r w_i\left[1 + \frac{c_{i\alpha}u_\alpha}{c_s^2}\right]. \tag{28}$$

For both models, the phase field is derived as

$$\phi = \frac{1}{r}\sum_i h_i. \tag{29}$$

Similarly to their Cartesian model (Sec. II B), they added a time derivative to their axisymmetric model and second-order velocity terms are not included in the equilibrium distribution function. In order to compare the axisymmetric interface tracking equations of models A and B, we use a BGK version of the hydrodynamic axisymmetric LB proposed in Ref. [31].

IV. NUMERICAL RESULTS

Seven distinct benchmark problems are designed to compare the accuracy of the presented LB models under varying Peclet numbers, density ratios, and viscosity ratios. Benchmark problems and their aims are summarized in Table I.

Models C and D are discussed in the following subsection. For interface tracking tests, the relative error is calculated

TABLE I. Benchmark problems and purposes.

Benchmark problem	Purpose
Moving bubble in a uniform vertical flow	Evaluate the accuracy of interface tracking of models A, B, C, and D
Moving bubble in a uniform diagonal flow	Evaluate the accuracy of interface tracking of models A, B, C, and D
Zalesak's a slotted disk rotation	Compare the accuracy of interface tracking of for the models A and B
Vortex drop	Compare the accuracy of interface tracking of for the models A and B
Static droplet	Investigate accuracy of multiphase models and test for spurious velocities
Bubble rising in a continuous phase	Evaluate the accuracy of two-phase flow in a realistic application
Static circular interface	Evaluate the accuracy of axisymmetric interface tracking models
Droplet oscillation	Validate axisymmetric multiphase models

TABLE II. The range of interfacial thickness, mobility, and density ratio.

Density ratio	Mobility (M)	Interface thickness (W)
1–10	0.01–0.02	3
10–100	0.02–0.03	4
100–1000	0.03–0.05	5

between the numerical results and initial condition by using this formula [14]:

$$||\delta\phi||_2 = \sqrt{\frac{\sum_{x,y}(\phi-\phi_0)^2}{\sum_{x,y}\phi_0^2}}, \tag{30}$$

where ϕ_0 is the initial value of the phase field. ϕ is defined such that $\phi_h - \phi_l = 1$ and we take $\phi_h = -\phi_l = 0.5$ for all of the interface tracking test problems [14,16]. When hydrodynamic effects are considered, $\phi_h = -\phi_l = 0.5$ can cause instabilities for high density ratios [32], and therefore $\phi_h = 1$, $\phi_l = 0$ is selected for the high-density-ratio cases of the static droplet, bubble rising in a continuous phase, and droplet oscillation tests.

The mobility and interface thickness are free parameters, whose values are dictated by considerations related to accuracy and stability. Choosing too small a value for interface thickness leads to numerical instabilities, especially for higher values of density ratio. On the other hand, it is desirable to use a sufficiently small interface to mimic a real sharp interface between two fluids in terms of preserving accuracy. Similarly, having too large a mobility leads to numerical dissipation, which is undesirable. Fakhari *et al.* [35], based on an extensive study, recommend interface thickness and mobility values for different ranges of density ratios as listed in Table II.

Here we focus on high-density-ratio simulations and so use $W = 5$ and $M = 0.03$–0.05. Also, numerically speaking, these LB models based on the CACE have the second-order convergence rates [14,16].

A. Results I: Interface-tracking equation

In this section, four LB models based on the CACE are considered in order to test the effects of the additional terms that emerge in model A. These models are shown in Table III. Model A is the model proposed by Geier *et al.* [14] and model B is the one proposed by Wang *et al.* [16] as we have discussed and presented so far. Model C is the recovered interface-tracking equation with only the additional temporal term and model D is the one with only the additional spatial derivative term. Models C and D will allow us to explore the explicit influence of the two additional terms.

The first four separate tests of Table I are considered. Various Peclet numbers (Pe) will be considered, where

$$\mathrm{Pe} = \frac{U_0 W}{M}, \tag{31}$$

where U_0 is the velocity in the y direction. All results are presented in terms of our characteristic advective timescale,

$$T_f = \frac{L_0}{U_0}, \tag{32}$$

where L_0 is the length of domain in terms of lattice cells. When we change the Peclet number in the presented cases, only U_0 varies and all other variables are kept constant.

1. Moving bubble in a uniform vertical flow

A circular interface (bubble) with radius $r = 25$ is located in a computational domain of size of $N_x \times N_y = 64 \times 384$, which is centered at $x_0 = 0$, $y_0 = 150$. Only half the domain is simulated and a symmetry boundary condition is imposed on the left ($x = 0$) and right boundaries. All other boundaries are treated as periodic. The mobility is set as $M = 0.03$ and the interface thickness as $W = 5$. A uniform vertical flow in the y direction of magnitude $U_0 = 0.03$ is specified. The starting phase field is given by

$$\phi(x,y) = 0.5 + 0.5\tanh\left[2\frac{r-\sqrt{(x-x_0)^2+(y-y_0)^2}}{W}\right], \tag{33}$$

In Fig. 1, the circular interface, $(\phi_h + \phi_l)/2$, is shown for $\mathrm{Pe} = 1$ at five different times ($t = 5T_f$, $t = 10T_f$, $t = 15T_f$, $t = 20T_f$, $t = 25T_f$); for all these times the bubble arrives at the same location. We find that the circular interfaces are almost identical for all of the cases in time up to $t = 25T_f$, which means that the additional terms do not seem to play an important role and are negligible for $\mathrm{Pe} = 1$.

As can be seen in Fig. 2, for $\mathrm{Pe} = 5$, the circular interfaces continue to have good agreement for models A and B, but the circular interface deviates from its initial shape for models C and D. Interestingly, although the manner of deviation seems opposite for each of these models, for model C, the interface is stretched in the x direction, while for model D, this stretch is in the y direction. Intuitively, this suggests that each of the additional terms has opposing effects, perhaps explaining why the results for models A and B are so similar. When Pe

TABLE III. Models and associated recovered interface-tracking equations.

Model	Recovered interface-tracking equation
A [14]	$\frac{\partial\phi}{\partial t} + \nabla\cdot(\phi\boldsymbol{u}) = \nabla\cdot\left[M(\nabla\phi - \lambda\boldsymbol{n})\right] + \nabla\cdot\left[\frac{\partial(\phi\boldsymbol{u})}{\partial t}\right]\frac{M}{c_s^2} + \nabla^2(\phi\boldsymbol{u}\boldsymbol{u})\frac{M}{c_s^2}$
B [16]	$\frac{\partial\phi}{\partial t} + \nabla\cdot(\phi\boldsymbol{u}) = \nabla\cdot[M(\nabla\phi - \lambda\boldsymbol{n})]$
C	$\frac{\partial\phi}{\partial t} + \nabla\cdot(\phi\boldsymbol{u}) = \nabla\cdot\left[M(\nabla\phi - \lambda\boldsymbol{n})\right] + \nabla\cdot\left[\frac{\partial(\phi\boldsymbol{u})}{\partial t}\right]\frac{M}{c_s^2}$
D	$\frac{\partial\phi}{\partial t} + \nabla\cdot(\phi\boldsymbol{u}) = \nabla\cdot[M(\nabla\phi - \lambda\boldsymbol{n})] + \nabla^2(\phi\boldsymbol{u}\boldsymbol{u})\frac{M}{c_s^2}$

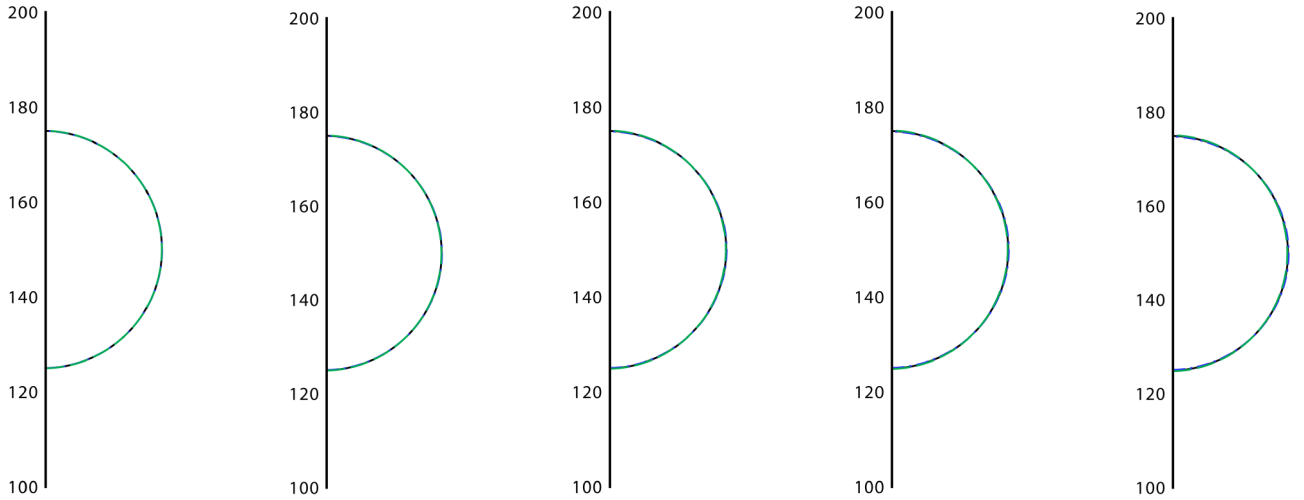

FIG. 1. Moving bubble in a uniform vertical flow. Model A is shown with a black solid line, model B is shown with a red dashed line, model C is shown with a blue dash-dot-dot line, and model D is shown with a green long-dashed line (all lines are on top of each others). Pe = 1. Left to right is $t = 5T_f$, $t = 10T_f$, $t = 15T_f$, $t = 20T_f$, and $t = 25T_f$.

increases to 20 (Fig. 3) a similar match between models A and B and mismatch for models C and D is observed, although at the latest time for model C a sharp point begins to emerge, which may be indicative of an instability.

Finally, for the last numerical experiment, Pe = 50 (Fig. 4), models A and B continue to be identical, while models C and D continue to cause stretching in opposite directions, however, with an additional unphysical undulation instability imposed. Again, the two additional terms appear to act opposite to one another, stabilizing the numerical solution.

The relative error for models A and B are provided in Table IV for varying Peclet numbers. It shows that the location of final interface and initial interface are in good agreement, however, more importantly, that any errors that do exist are virtually identical for both cases with only negligible gain from model B. Errors for cases C and D are not presented as these are clearly unphysical and are only shown to demonstrate the balancing nature of the additional two terms in model A.

2. *Moving bubble in a uniform diagonal flow*

The next case study is diagonal translation of a circular interface. A circular interface is placed in a constant velocity field $\boldsymbol{u} = (U_0, U_0)$ in the corner of a computational domain of size $N_x \times N_y = 200 \times 200$. The interface thickness and characteristic length are $W = 5$ and $\frac{W}{L_0} = 0.025$, respectively. The periodic boundary conditions are imposed on all boundaries. The circular interface after $t = 10T_f$ is shown in Figs. 5(a) and 5(b) for Pe = 5 and Pe = 50, respectively. For Pe = 5, the interface location for all models agree closely, which is consistent with the previous numerical experiment. For Pe = 50, the interfaces for cases C and D deviate, while A and B remain very similar. Again, the deviation of models C and D appears to be in opposition to one another, reinforcing that the

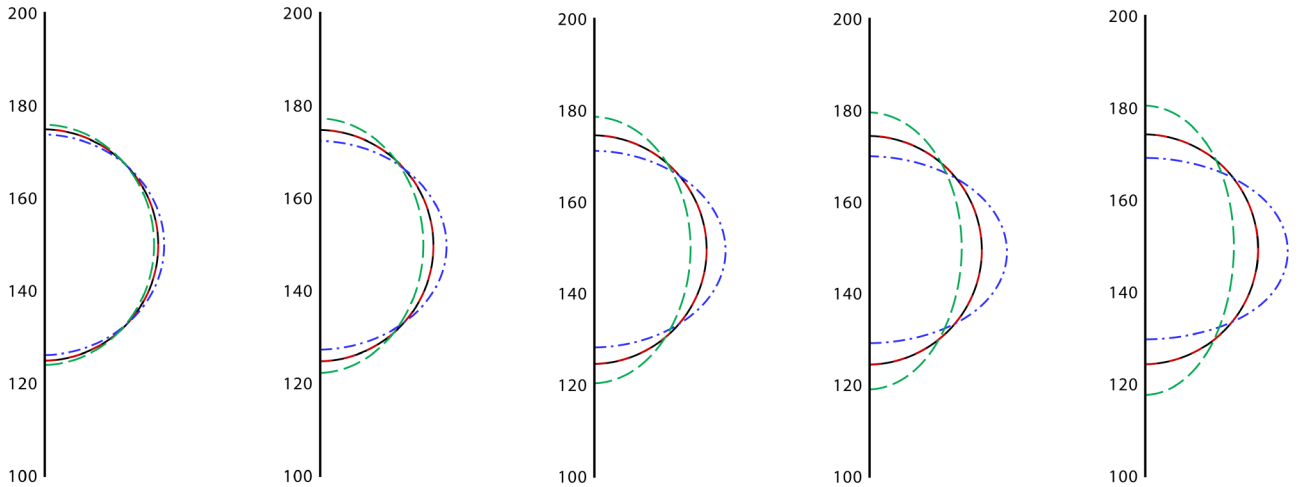

FIG. 2. Moving bubble in a uniform vertical flow. Model A is shown with a black solid line (circular shape in the center), and model B is shown with a red dashed line (circular shape in the center). Models A and B are on top of each other. Model C is shown with a blue dash-dot-dot line (horizontal elliptical shape), and model D is shown with a green long-dashed line (vertical elliptical shape). Pe = 5. Left to right is $t = 5T_f$, $t = 10T_f$, $t = 15T_f$, $t = 20T_f$, and $t = 25T_f$.

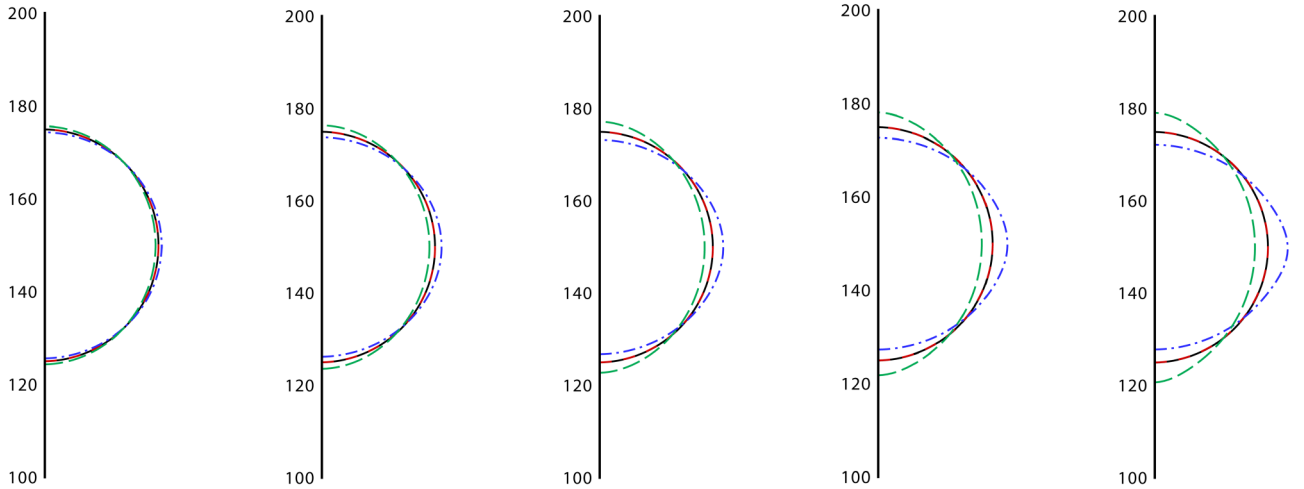

FIG. 3. Moving bubble in a uniform vertical flow. Model A is shown with a black solid line (circular shape in the center), and model B is shown with a red dashed line (circular shape in the center). Models A and B are on top of each other. Model C is shown with a blue dash-dot-dot line (horizontal elliptical shape), and model D is shown with a green long-dashed line (vertical elliptical shape). Pe = 20. Left to right is $t = 5T_f$, $t = 10T_f$, $t = 15T_f$, $t = 20T_f$, and $t = 25T_f$.

two additional terms in model A balance and cancel each other out. The results here are consistent with the last numerical experiment.

For the evaluation of the accuracy of the models, the relative error for models A and B are shown in Table V. The errors are small and very close for both models, although model B does marginally outperform model A.

In the following, an analysis of the additional terms related to model A is performed to further investigate their effects. These additional terms can be written as follows:

$$\frac{M}{c_s^2}\nabla\cdot\left[\frac{\partial(\phi\boldsymbol{u})}{\partial t}+\nabla(\phi\boldsymbol{u}\boldsymbol{u})\right]=\frac{M}{c_s^2}\nabla\cdot\left\{\boldsymbol{u}\left[\frac{\partial\phi}{\partial t}+\nabla\cdot(\phi\boldsymbol{u})\right]+\phi\left(\frac{\partial\boldsymbol{u}}{\partial t}+\boldsymbol{u}\cdot\nabla\boldsymbol{u}\right)\right\}. \quad (34)$$

This shows the additional terms can be written in a manner composed of $[\frac{\partial\phi}{\partial t}+\nabla\cdot(\phi\boldsymbol{u})]$, which is equal to the left-hand side of the CACE [see Eq. (1)], and $(\frac{\partial\boldsymbol{u}}{\partial t}+\boldsymbol{u}\cdot\nabla\boldsymbol{u})$, which is equal to the left-hand side of momentum equation [see Eq. (4)]. Hereafter, $\nabla\cdot\{\boldsymbol{u}[\frac{\partial\phi}{\partial t}+\nabla\cdot(\phi\boldsymbol{u})]\}$ is referred to as part 1 of the additional terms and $\nabla\cdot[\phi(\frac{\partial\boldsymbol{u}}{\partial t}+\boldsymbol{u}\cdot\nabla\boldsymbol{u})]$ as part 2. As shown in Ref. [35], this LB model is valid for Mach number ($\mathrm{Ma}=\frac{|\boldsymbol{u}|}{c_s}$) less than $\mathrm{Ma}<0.3$ when it pairs with the hydrodynamic equations. If, however, the LB model corresponding to the interface-tracking equation is solved in the absence of the N-S equation (e.g., an externally imposed independent flow field as in the above tests), it can provide stable solutions for $\mathrm{Ma}>0.3$ depending on the choice of mobility (see Table II). Based on numerical experimentation and experience, the solution is stable for $\mathrm{Ma}<0.7$ for a

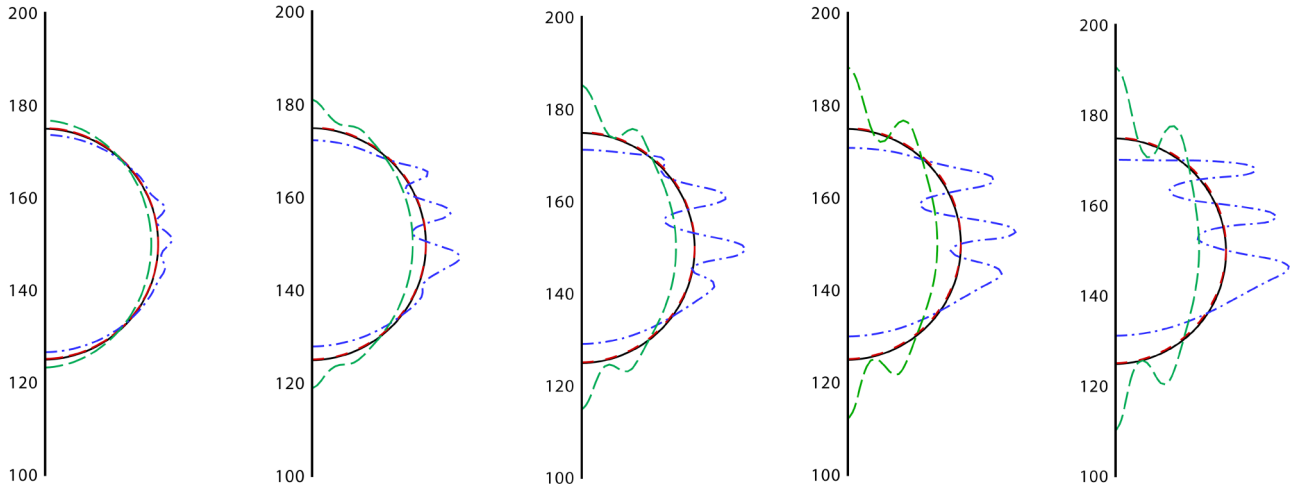

FIG. 4. Moving bubble in a uniform vertical flow. Model A is shown with a black solid line (circular shape in the center), and model B is shown with a red dashed line (circular shape in the center). Models A and B are on top of each other. Model C is shown with a blue dash-dot-dot line (irregular shape expanded in the x direction), and model D is shown with a green long-dashed line (irregular shape expanded in the y direction). Pe = 50. Left to right is $t = 5T_f$, $t = 10T_f$, $t = 15T_f$, $t = 20T_f$, and $t = 25T_f$.

TABLE IV. Relative error of the two models for the moving bubble in a uniform vertical flow test.

Model	Pe = 1	Pe = 5	Pe = 20	Pe = 50
A	0.0001	0.0012	0.0043	0.0067
B	0.0001	0.0012	0.0042	0.0064

TABLE V. Relative error of the two models for the moving bubble in a uniform diagonal flow test.

Model	Pe = 5	Pe = 50
A	0.0004	0.0038
B	0.0004	0.0032

mobility of $M = 0.03$ (see Sec. IV A 1 Pe = 50). In order to consider hydrodynamic effects in the two-phase model, the velocity of the flow field should be less than 0.1732 due to the Mach number restriction Ma < 0.3. Here, let us assume that part 2 of the additional terms is negligible (see Appendix C) and Eq. (34) is reduced to

$$\frac{M}{c_s^2}\nabla\cdot\left[\frac{\partial(\phi\boldsymbol{u})}{\partial t}+\nabla(\phi\boldsymbol{u}\boldsymbol{u})\right]=\frac{M}{c_s^2}\nabla\cdot\left\{\boldsymbol{u}\left[\frac{\partial\phi}{\partial t}+\nabla\cdot(\phi\boldsymbol{u})\right]\right\}. \tag{35}$$

In order to analyze the new form of these additional terms, we invoke dimensional analysis. Length and velocity scales are given by L and U, respectively. Therefore, the corresponding advective timescale is $T = L/U$. All scales are chosen such that the normalized variables are on the order unity. For instance $\boldsymbol{u}^* = u/U$, $\nabla^* = \nabla L$, and $t^* = tU/L$. Therefore, the nondimensional form of the partial differential equation (PDE) corresponding to model A (see Table III) can be written as:

$$\frac{\partial\phi}{\partial t^*}+\nabla^*\cdot(\phi\boldsymbol{u}^*)=\frac{1}{\mathrm{Pe}}\nabla^*\cdot\left\{\left[\nabla^*\phi-\frac{1-4(\phi-\phi_0)^2}{W^*}\boldsymbol{n}\right]\right\}+\frac{\mathrm{Ma}^2}{\mathrm{Pe}}\nabla^*\cdot\left\{\boldsymbol{u}^*\left[\frac{\partial\phi}{\partial t^*}+\nabla\cdot(\phi\boldsymbol{u}^*)\right]\right\}. \tag{36}$$

Based on the nondimensional CACE, one can write the additional terms as:

$$\frac{\mathrm{Ma}^2}{\mathrm{Pe}}\nabla^*\cdot\left\{\boldsymbol{u}^*\left[\frac{\partial\phi}{\partial t^*}+\nabla^*\cdot(\phi\boldsymbol{u}^*)\right]\right\}=\frac{\mathrm{Ma}^2}{\mathrm{Pe}}\nabla^*\cdot\left(\boldsymbol{u}^*\frac{1}{\mathrm{Pe}}\nabla^*\cdot\left\{\left[\nabla^*\phi-\frac{1-4(\phi-\phi_0)^2}{W^*}\boldsymbol{n}\right]\right\}\right). \tag{37}$$

Therefore, this part of the additional terms, $[\frac{\partial\phi}{\partial t^*}+\nabla^*\cdot(\phi\boldsymbol{u}^*)]$, has a relationship with $O(\frac{1}{\mathrm{Pe}})$. To analyze these error terms carefully, two regimes of Peclet number are considered. The first regime is Pe $\sim O(1)$ and the second regime is Pe $\gg O(1)$.

(i) Pe $\sim$ **O(1)**: In the first regime, advection and diffusion effects are comparable. To implement small Peclet number, the velocity magnitude should be set based on the limitations of the numerical method associated with the mobility and the interface thickness [35], as previously explained in Sec. IV. The resulting velocity magnitude will be small for the cases presented. Consequently, the Mach number is small (Ma $\ll 1$) and the error terms that have a second-order relationship with Mach number should be negligible. Thus, the additional terms for models A, C, and D are very small and all of the models are roughly identical in terms of predicting the interface.

(ii) Pe $\gg$ **O(1)**: In the second regime, the Peclet number is relatively large and the advection term is dominant. In order

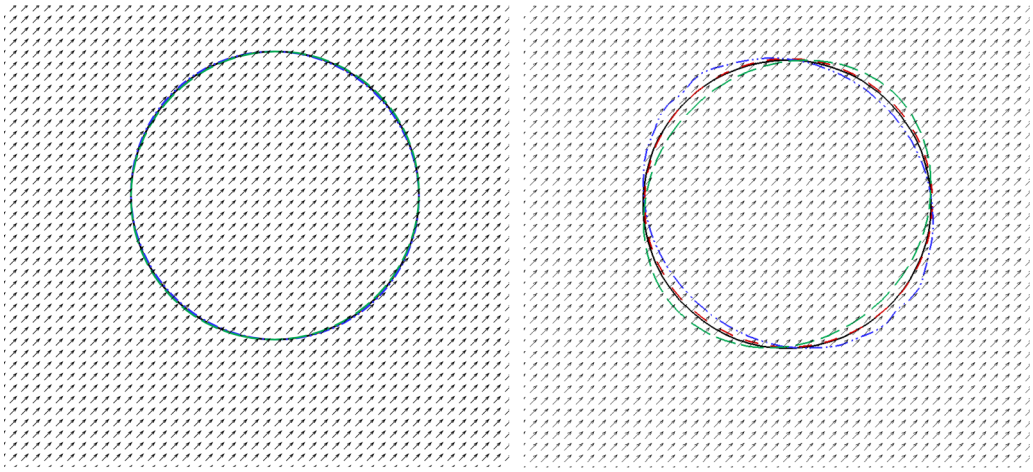

(a) (b)

FIG. 5. Moving bubble in a uniform diagonal flow at $t = 10T_f$. (a) Pe = 5 and (b) Pe = 50. Model A is shown with a black solid line (circular shape in the center), and model B is shown with a red dashed line (circular shape in the center). Models A and B are on top of each other. Model C is shown with a blue dash-dot-dot line, and model D is shown with a green long-dashed line (figure is a zoom-in). (a) All the lines are on top of each other. (b) Models A and B are on top of each other. Model C is a horizontal elliptical shape when the x axis rotates 135° counterclockwise. Model D is a horizontal elliptical shape when the x axis rotates 45° counterclockwise.

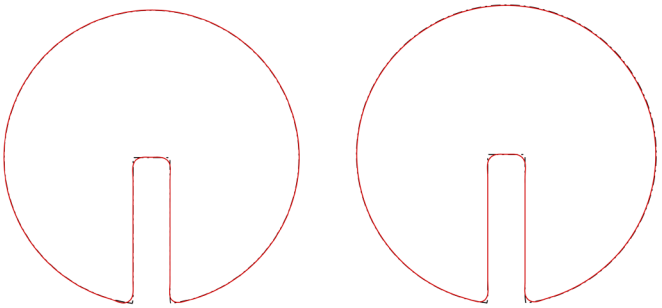

FIG. 6. Zalesak's disk at Pe = 75. (a) Model A. (b) Model B. Black solid line is initial condition and red line is $t = T_f$. Lines are on top of each other.

to increase the Peclet number, the velocity magnitude should be larger than in regime (i); again due to the restrictions on mobility and interface thickness [32,35], the velocity should be larger than the first regime in order to increase the Peclet number. Therefore, the additional terms are not negligible due to having a larger Mach number. If we keep one of the additional terms $\{(\frac{\partial\phi}{\partial t^*})$ or $[\nabla^* \cdot (\phi \boldsymbol{u}^*)]\}$, then these terms are not small anymore. However, regardless of $\frac{\mathrm{Ma}^2}{\mathrm{Pe}}$, as seen from Eq. (37) the new form of additional terms scale as $(\frac{1}{\mathrm{Pe}})$. As a result, for large Peclet number, error terms $[\frac{\partial\phi}{\partial t^*}$ and $\nabla^* \cdot (\phi \boldsymbol{u}^*)]$ should cancel each other out as the right-hand side of Eq. (37) is very small $(\frac{1}{\mathrm{Pe}} \ll 1)$.

In the numerical experiment of a moving bubble in a uniform flow (see Sec. IV A 1), the flow field is steady state and constant. Therefore, part 2 of the additional terms is zero. For this test, two regimes of Peclet number are considered to analyze the additional terms. In the first regime, Pe $\sim$ 1; to keep Pe = 1, the velocity magnitude is set to $U_0 = 0.006$. As a result, Ma = 0.0104. Because the error terms are proportional to $\frac{\mathrm{Ma}^2}{\mathrm{Pe}} = 11 \times 10^{-5}$, they become negligible. As we expect, the additional terms for models A, C, and D are very small and all of the models are roughly identical in terms of predicting the interface. In the second regime, Pe $\gg O(1)$, the case with Pe = 50 is considered, and therefore the velocity magnitude is set to $(U_0 = 0.3$ m/s). As a consequence, the Mach number is Ma = 0.5196 and the additional terms are proportional to $\frac{\mathrm{Ma}^2}{\mathrm{Pe}} = 5.4 \times 10^{-3}$. This Mach number is one order of magnitude greater than the first regime. Therefore, models C and D cannot capture the interface as the error terms are not small; however, these error terms do cancel each other out for model A because of the large Peclet number. This is consistent with our results (see Fig. 4 for model A). Consequently, model A captures the interface almost identically to model B.

From the above discussion, it can be concluded that models C and D cannot capture the interface accurately for large Peclet number; however, model A and B can predict near-identical interfaces for varying Peclet numbers. When a hydrodynamics effect is considered, the Mach number is less than 0.3 due to numerical method restrictions [35]. Because of the relationship of the additional terms with $\frac{\mathrm{Ma}^2}{\mathrm{Pe}}$, these additional terms are in the range of first regime and they should be negligible. Therefore, from here onward, only models A and B will be considered.

3. Zalesak's a slotted disk rotation

A very common test for validation of interface tracking is the Zalesak's rotation of a slotted disk [38]. As an initial condition, a slotted disk of radius $r = 80$ is placed in the center of a periodic computational domain of size $L_0 \times L_0 = 200 \times 200$. A slot width of 20 is placed in the center of the disk and the height of slot (h) is 80 $(h = r)$. The interface thickness and characteristic length are $W = 5$ and $\frac{W}{L_0} = 0.025$, respectively. A rotational velocity, given by

$$u_x = -U_0\pi\left(\frac{y}{L_0} - 0.5\right), \qquad u_y = U_0\pi\left(\frac{x}{L_0} - 0.5\right), \quad (38)$$

is imposed.

The initial interface and interface at time $t = T_f$ (one full rotation) are shown in Fig. 6. It can be seen that for both models A and B, the final shape of interface is in good agreement with the initial condition.

In Fig. 7 the time evolution of the Zalesak's disk for Pe = 75 for models A and B is shown to compare the accuracy of these models qualitatively. Visually, the results are almost indistinguishable. To further investigate the accuracy of these models, the height of slot is increased to 105 lattice $(h = 1.3125r)$. The time evolution of disk is shown in Fig. 8. It can be seen that despite of narrow height of the disk, there is no oscillation on the interface and both of the models are stable. The relative error at different times is tabulated in Table VI, which shows that the two models produces almost the same error.

4. Vortex drop

A common benchmark problem to test the accuracy of two-phase flow is the so-called vortex drop. This test problem highlights the accuracy of two-phase models by requiring resolution of thin filaments, which arise due to stretching

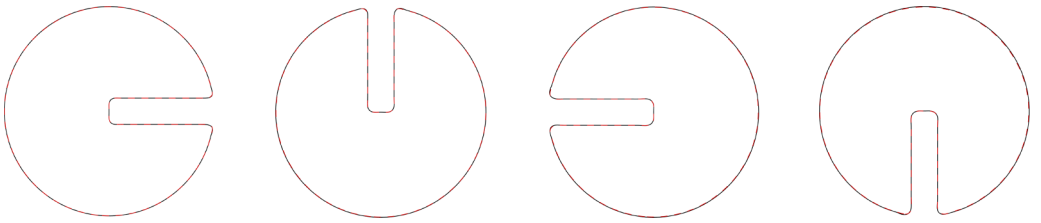

FIG. 7. Rotation of disk with time. Left to right is $t = \frac{1}{4}T_f$, $t = \frac{1}{2}T_f$, $t = \frac{3}{4}T_f$, and $t = T_f$. The black line is model A and the red line is model B. Lines are on top of each other.

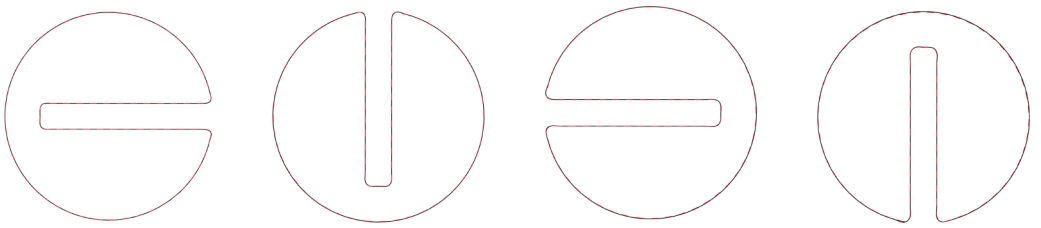

FIG. 8. Rotation of disk with time. Left to right is $t = \frac{1}{4}T_f$, $t = \frac{1}{2}T_f$, $t = \frac{3}{4}T_f$, and $t = T_f$. The black line is model A and the red line is model B. Lines are on top of each other.

and tearing processes. Initially, a circular drop is placed off-center in an oscillatory vortex. The oscillatory velocity field is defined as:

$$u_x = \cos^2\left(\pi\frac{x-x_0}{L_0}\right)\sin\left(2\pi\frac{y-y_0}{L_0}\right)\cos\left(\frac{\pi t}{T_f}\right),$$
$$u_y = \cos^2\left(\pi\frac{y-y_0}{L_0}\right)\sin\left(2\pi\frac{x-x_0}{L_0}\right)\cos\left(\frac{\pi t}{T_f}\right), \quad (39)$$

where T_f is the nondimensional time and $x_0 = \frac{L_0}{2}$, $y_0 = \frac{3L_0}{4}$. U_0 is set to 0.1. The initial radius of the interface is $r = \frac{L_0}{8}$ and the interface thickness is set to $W = 5$. The domain size is $L_0 \times L_0$. At $t = 0.5T_f$ the reversed velocity is imposed, aiming to bring the stretched drop back to its initial location at $t = T$. The $\cos(\frac{\pi t}{T_f})$ term reverses the velocity field smoothly.

The evolution of the drop is shown in Fig. 9 for different resolutions. The results show the initial shape of drop is preserved at final time $t = T_f$ with some noticeable oscillations for the relatively coarser grids. The relative error for

TABLE VI. Relative error of the two models for the Zalesak's a slotted disk rotation test.

Model	$t = \frac{1}{4}T_f$	$t = \frac{1}{2}T_f$	$t = \frac{3}{4}T_f$	$t = T_f$
A : $h = r$	0.0011	0.0026	0.0046	0.0070
B : $h = r$	0.0011	0.0026	0.0046	0.0070
A : $h = 1.3125\,r$	0.0014	0.0030	0.0053	0.0079
B : $h = 1.3125\,r$	0.0014	0.0031	0.0054	0.0080

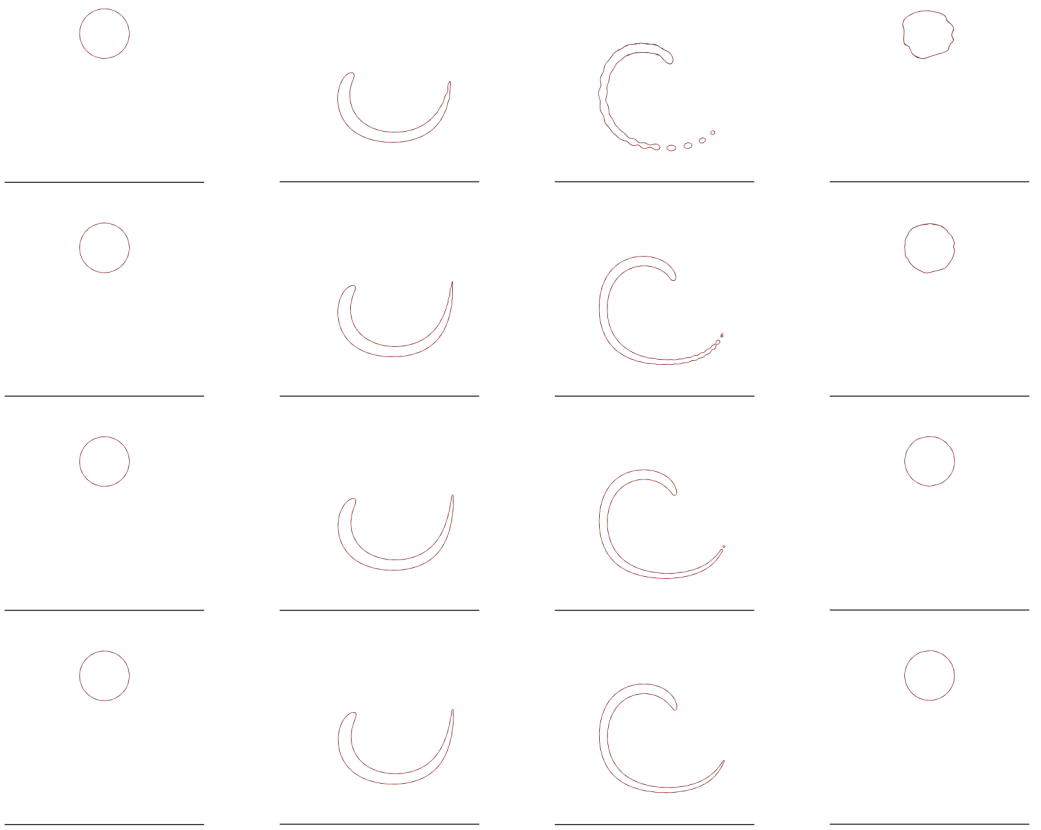

FIG. 9. Time evolution of the vortex drop. Left to right is $t = 0$, $t = \frac{1}{4}T_f$, $t = \frac{1}{2}T_f$, $t = T_f$. Top to bottom $L_0 = 100$ ($\frac{W}{L_0} = 0.05$), $L_0 = 200$ ($\frac{W}{L_0} = 0.025$), $L_0 = 400$ ($\frac{W}{L_0} = 0.0125$), $L_0 = 800$ ($\frac{W}{L_0} = 0.00625$). The black line is model A and the red dashed line is model B. Lines are on top of each other.

TABLE VII. Relative error of the two models for the vortex drop test.

Model	$L_0 = 100$	$L_0 = 200$	$L_0 = 400$	$L_0 = 800$
A	1.245	1.1100	0.5305	0.1404
B	1.244	1.1100	0.5306	0.1404

different resolutions is shown in Table VII. The errors for model A and model B are virtually identical.

B. Results II: Interface-tracking equation coupled with the hydrodynamic equation

In the following examples, hydrodynamic effects are also considered. Two cases are chosen: a static droplet test, a common benchmark for LB models, and a bubble rising in a continuous phase, which is a more realistic flow example, demonstrating the ability to simulate a complex flow of practical interest. Note that the Cartesian formulation of the hydrodynamic axisymmetric LB proposed in Ref. [31] is used in this part.

1. Static droplet

The static droplet is widely used to validate multiphase models [17,39,40]. Here we will simulate this problem with a large density ratio. A stationary droplet is located at the center of a computational domain of size $N_x \times N_y = 100 \times 100$. The radius of the droplet is $R = 25$, the interface thickness is $W = 5$, and the characteristic length is $\frac{W}{L_0} = 0.05$. The boundary conditions are set as bounce back (no-slip boundary) on all boundaries. The initial phase field variable is set as

$$\phi(x, y) = 0.5 + 0.5 \tanh\left[2\frac{R - \sqrt{(x - x_0)^2 + (y - y_0)^2}}{W}\right], \tag{40}$$

The density ratio is set to $\frac{\rho_h}{\rho_l} = 1000$ and $\nu_h = \nu_l = 0.1$ and $M = 0.03$.

Figure 10 shows the interface after 500 000 iterations and it is immediately obvious that there is good agreement for both models A and B with the initial interface. This demonstrates that mass is well conserved for both models A and B, as the location of the initial interface is identical to the final interfaces. The relative error for the both models are shown in Table VIII.

In many LB frameworks, spurious velocities occur near interfaces, which is a problem for two-phase flows. Generally this velocity can be eliminated by using a potential form of surface tension force and a mixed finite-difference scheme [8]. For this benchmark, the magnitude of this velocity is

TABLE VIII. Relative error of the two models for the static droplet test.

Model	$t = 500\,000$
A	0.0004
B	0.0004

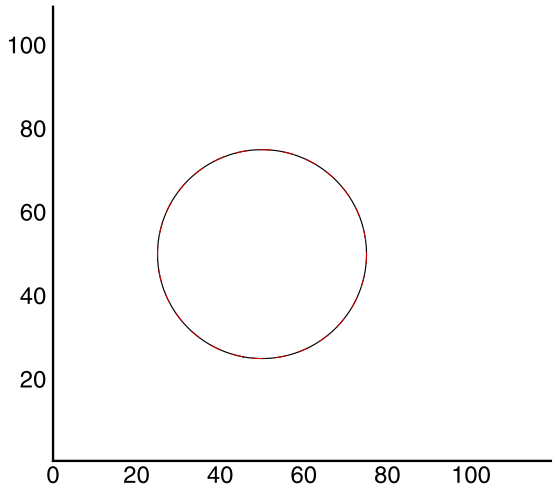

FIG. 10. The phase-field contour after 5 000 000 iterations is shown. Model A is shown with a black solid line, model B is shown with a red dashed line, and the initial condition is denoted with a black dot. Lines are on top of each other.

computed by $|\boldsymbol{u}|_{\max} = (\sqrt{u_x^2 + u_y^2})_{\max}$ and for both models A and B the maximum spurious velocity is on the order of 10^{-6}.

2. Bubble rising in a continuous phase

Next we consider the case of a single rising bubble under buoyancy, which has received much previous attention, both numerically and experimentally [21,41,42]. This problem is generally classified in terms of two dimensionless parameters, the Bond number, Bo, and Morton number, Mo, which are defined as [21,22]

$$\mathrm{Bo} = \frac{g\rho_h D^2}{\sigma}, \qquad \mathrm{Mo} = \frac{g\mu_h^4}{\rho_h \sigma^3}, \tag{41}$$

where g is gravitational acceleration, D is the initial diameter of the bubble, and μ is the dynamic viscosity. The Reynolds number, Re, can be computed from the relation $\mathrm{Mo} = \frac{\mathrm{Bo}^3}{\mathrm{Re}^4}$.

The size of computational domain is $N_x \times N_y = 200 \times 800$. The radius of the initial bubble is 50 and is located at (0,100). The left vertical boundary at $x = 0$ is treated as symmetric; periodic boundary conditions are imposed on the top and bottom with a no slip boundary on the right vertical side for the hydrodynamic LB equation. For the LB phase-field equation, top and bottom boundary conditions are periodic, the left side is set to be symmetric, and a no flux boundary condition is imposed on the right vertical side of the domain. Other parameters are set as $W = 5$, $M =$

TABLE IX. Several cases for bubble rising in a continuous phase test with density ratio $\frac{\rho_h}{\rho_l} = 1000$.

Case	Bo	Mo	Re	ν_h	ν_l	g
A1	32.2	8.2×10^{-4}	79.88	0.025	0.25	4.0×10^{-6}
A2	243	266	15.24	0.0656	0.656	1.0×10^{-6}
A3	641	43.1	49.72	0.06	0.6	9.0×10^{-6}
A4	116	4.63×10^{-3}	135.5	0.0184	0.184	6.25×10^{-6}

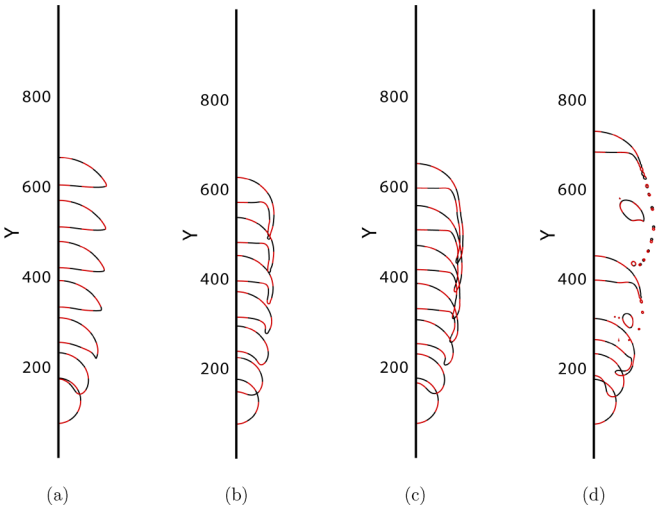

FIG. 11. Evolution of bubble rising in a continuous phase. Left to right is (a) case A1, (b) case A2, (c) case A3, and (d) case B4. Nondimensional times for (a), (b), and (c) are $t^* = 0$, 1.5, 3, 4.5, 6, and 7.5 and for (d) are $t^* = 0$, 1.5, 3, 5.5, and 10. Solid black line is model A and dashed red line is model B. Lines are on top of each other.

0.03, and $\frac{W}{L_0} = 0.00625$. The density ratio is 1000 and other important parameters are presented in Table IX. Figure 11 shows the temporal evolution of bubble shapes for the four cases presented in Table IX. For all cases, the initial bubble rises with interface deformation until reaching its equilibrium shape. As with previous examples for all cases and all times, any differences between model A and model B are almost negligible.

To demonstrate the ability of the presented LB models to capture realistic interfaces, the terminal shape of bubbles are compared to experimental results from Ref. [41] and front tracking simulation results from Ref. [21] in Table X. Generally our predictions are in good agreement with these experimental measurements and classical numerical predictions. However, there are some minor deviations (although more significant than the very minor differences between models A and B).

Finally, as noted in Table XI in our simulations the mass ratio ($\frac{\text{InitialMass}}{\text{FinalMass}}$) of the system is roughly constant for both models across different conditions (A1, A2, A3, and A4), meaning mass is well conserved for both model A and model B.

It can be concluded that model A and model B can capture the interface for the complex bubble dynamics fairly accurately.

TABLE X. Terminal bubble shapes observed in experiments predicted by front tracking method and LB methods. The solid black line is model A and the solid red line is model B. Lines are on top of each other.

Case	A1	A2	A3	A4
Experiment [41]	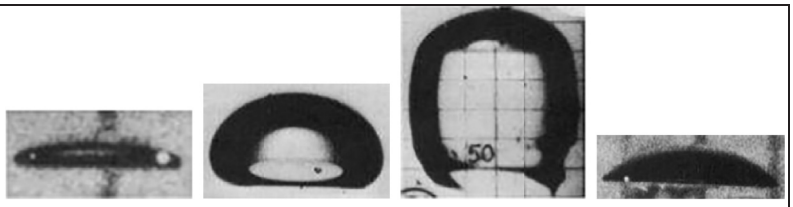			
Front tracking [21]				
LBM	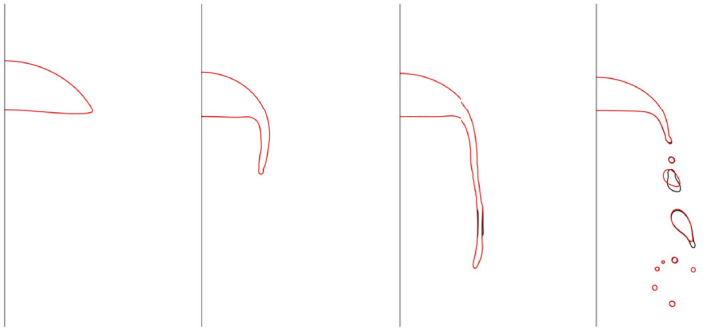			

TABLE XI. Mass ratio for the two models at different cases for the bubble rising in a continuous phase test.

Model	A1	A2	A3	A4
A	1.000000107	1.000000058	1.000000112	1.000000226
B	1.000000107	1.000000058	1.000000112	1.000000226

C. Results III: Axisymmetric model

In this section, in order to investigate the accuracy of axisymmetric models in terms of interface tracking, the presented LB model (model A) as well as the model proposed by Liang *et al.* [31] (model B) are considered for two basic benchmark problems.

Note that model B contains two time-dependent terms on the source term of LB equation. However, the presented axisymmetric model (model A) does not include these time-dependent terms due to these terms are relatively small [see Eq. (27)]. Thus, the proposed axisymmetric model outperforms on the so-called improved models in terms of efficiency, particularly on distributed parallel machines.

1. Static circular interface

To test the accuracy of axisymmetric interface model, a semicircular interface is placed on the axis of a computational domain. The system is static with no flow. Therefore, the semicircular interface should stay in the same location and the mass should remain constant throughout the simulation. However, in our investigation we notice that the mass reduces over time. To investigate this problem for axisymmetric models, a semicircular interface with five different mesh grid resolutions is considered and the interface is compared to the initial condition after 39 000 iterations with interface thickness of $W = 5$. The computational domain is $N_r \times N_z = L_0/2 \times L_0$ and the initial interface radius is $L_0/4$. Time evolution of the normalized mass, $M/M_0 = \frac{\text{Mass}(t)}{\text{Mass}(0)}$, and RMS error [see Eq. (30)] for both models are shown in Fig. 12 and Table XII, respectively. In all presented cases, the results between models A and B are virtually identical, as before. However, as can be

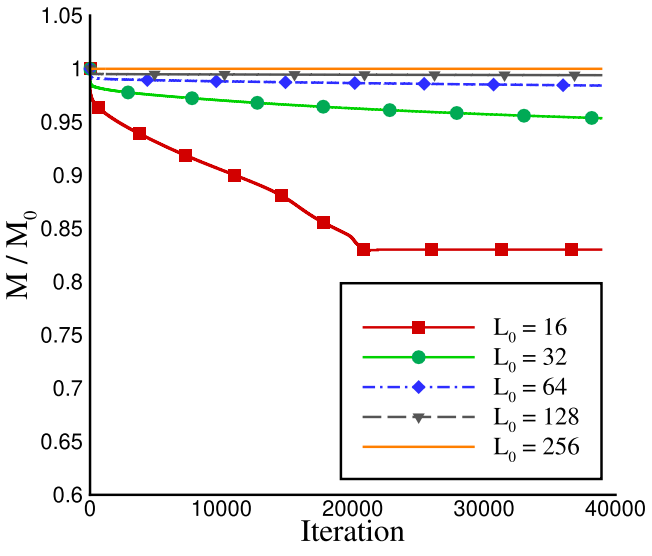

FIG. 12. Time history of the normalized mass for both models.

TABLE XII. RMS of the two models for the static circular interface test.

Model	$L_0 = 16$	$L_0 = 32$	$L_0 = 64$	$L_0 = 128$	$L_0 = 256$
A	0.3477	0.0919	0.02974	0.0081	0.0022
B	0.3478	0.0919	0.02974	0.0081	0.0022

seen in Table XII, for the $L_0 = 16$ case, the RMS error for model A and B is starkly large. As the number of grid points increases the RMS error becomes small; however, there is still a reduction in mass. For the case $L_0 = 16$, the mass of the system reduces tremendously to almost 82% its initial value, while for $L_0 = 256$ the maximum change in mass is in the order of 0.1%, which is negligible. To the authors' knowledge, this lack of mass conservation in axisymmetric phase-field methods has not been addressed in the literature so far. In the following, we investigate the underlying reasons causing this issue.

In the A-C equations (1) or (18) and (19), the λn term on the right-hand side is supposed to impose a predefined interface profile, obtained from minimization of free energy of the system [14]. At equilibrium, the interface profile reaches this predefined profile and on the right-hand side these equations theoretically becomes zero. However, in a numerical setup this does not happen due to the numerical calculation of the gradient term and round-off errors. In systems with the Cartesian coordinate system [Eq. (1)], this issue is not seen as significant [14]. However, under axisymmetric coordinate things are different [Eqs. (18) and (19)]. Without loss of generality, we assume that the velocity is zero everywhere and that the interface is parallel to the z axis. Therefore, Eq. (18) [the same explanation holds for Eq. (19)] can be simplified to

$$\partial_t \phi = \partial_r [M(\partial_r \phi - \lambda n_r)] + \frac{M}{r}(\partial_r \phi - \lambda n_r). \tag{42}$$

Comparing Eq. (42) with its counterpart in a Cartesian coordinate system, we find that the last term on the right-hand side is a additional term due to the transformation: We posit that it causes the mass conservation violation. At equilibrium, the interface profile can be expressed as a hyperbolic tangent [14]:

$$\phi^{\text{eq}} = \phi_0 \pm \phi_0 \tanh\left[\frac{2(r - r_0)}{W}\right], \tag{43}$$

where r_0 is the radial distance corresponding to ϕ_0. Evaluating the additional term for the equilibrium profile gives

$$\frac{M}{r}(\partial_r \phi^{\text{eq}} - \lambda n_r) = 0, \tag{44}$$

where $n_r = \pm 1$. In a numerical setup, however, the above equation cannot be zero and, in contrast to a Cartesian system, its value depends on r such that it exponentially approaches zero as r increases. To show this more clearly, consider two different locations of the interface, i.e., $r_0 = 10$ and $r_0 = 20$. Figure 13(a) shows the interface profile and the value of the additional terms as functions of r for $M = 0.03$ and $W = 5$. As can be seen clearly in Fig. 13(a), the further the interface gets away from the axis, the less the value of this additional term will be. This is why having a higher grid resolution helps

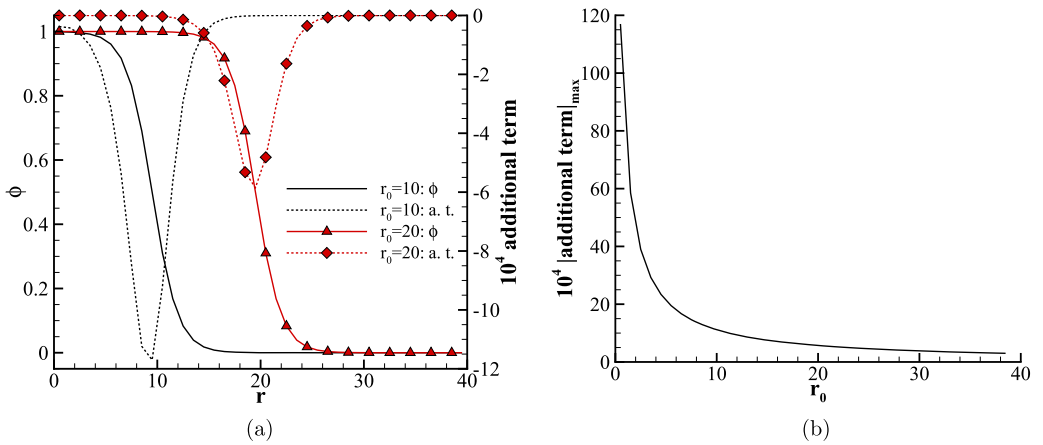

FIG. 13. (a) Profile of the phase field and additional term as a function of r for two different interface locations of $r_0 = 10$ and $r_0 = 20$. (b) Highest absolute value of the additional term for different interface locations.

yield better mass conservation, although it must be noted that the axisymmetric equation never stops violating mass conservation as long as resolution is finite. This is consistent with our observations.

Figure 13(b) shows the highest absolute value of the additional term as a function of r_0 for the same value of mobility and interface thickness as before. In summary, a phase-field equation cannot conserve mass in its asymmetric form despite its conservative nature in the Cartesian system. To tackle this issue, Huang *et al.* [22] introduced a mass correction step to bring back the lost mass to the domain. However, this is an algorithmic correction that empirically makes the model work rather than one based on sound physical and mathematical reasoning, meaning that extrapolation to more complex problems may not be straightforward.

2. Droplet oscillation

One of the typical classic validations for axisymmetric multiphase LB models is droplet oscillation [27,43,44]. If a liquid droplet is distorted from a circular shape into an ellipse, then the droplet develops oscillatory behavior before settling back to the original circular shape. Miller and Scriven [45] presented a semianalytical solution for the oscillation frequency of the nth mode of the droplet,

$$\omega_n = \omega_n^* - 0.5\alpha\sqrt{\omega_n^*} + 0.25\alpha^2, \tag{45}$$

where ω_n^*, the natural resonance frequency, is given by

$$\omega_n^* = \sqrt{\frac{n(n-1)(n+1)(n+2)}{R_e^3[n\rho_l + (n+1)\rho_h]}\sigma}, \tag{46}$$

where R_e is the equilibrium radius of the droplet and α is the viscosity contribution defined as [45]

$$\alpha = \frac{(2n+1)^2\rho_h\rho_l\sqrt{\nu_h\nu_l}}{\sqrt{2}R_e[n\rho_l + (n+1)\rho_h](\rho_h\sqrt{\nu_h} + \rho_l\sqrt{\nu_l})}, \tag{47}$$

where n is the mode of oscillation. The second mode of oscillation ($n = 2$) is considered here [31,43].

The computational domain is $N_r \times N_z = 200 \times 100$ and an ellipsoidal droplet with the ratio of $R_r = 25$, $R_z = 85$ is placed at the center of domain (100,0). The density ratio is $\frac{\rho_h}{\rho_l} = 1000$ and other important simulation parameters are fixed as $W = 5$, $\frac{W}{L_0} = 0.0125$, $\sigma = 0.3$, $M = 0.03$, $\nu_h = 6 \times 10^{-3}$, $\nu_l = 6 \times 10^{-2}$. The droplet evolution in time is shown in Fig. 14. Again, the droplet behavior is consistent for models A and B for all time steps.

The deviation of mass is less than 0.5%, which suggests that the grid size may be sufficient for this simulation.

The variation of the half-axis length R_r versus time is shown in Fig. 15, where the results with other initially given values of $R_r = 30, 45, 60$ are also presented to examine the effect of droplet size. Figure 15 shows that the amplitude of the oscillation normalized by the corresponding equilibrium radius R_e fluctuates around 1 for all cases, and as expected, the dimensionless maximum amplitude is reduced for a larger droplet size.

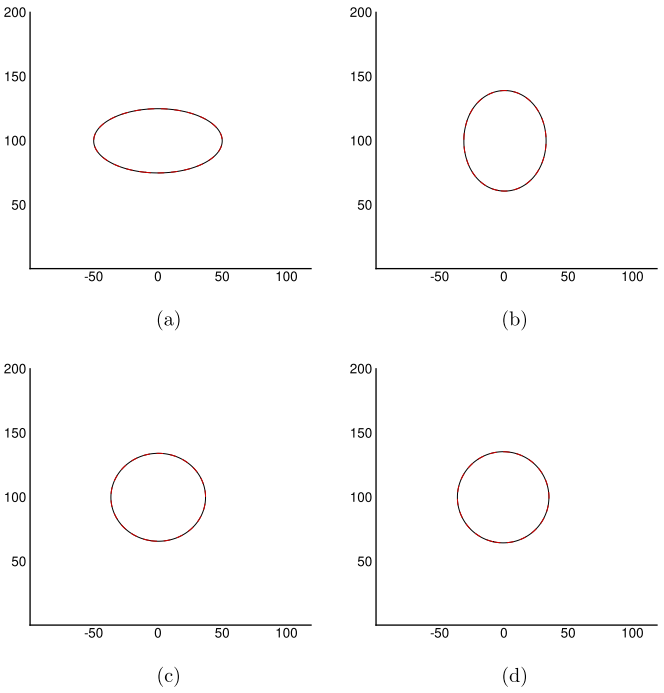

FIG. 14. Evolution of droplet oscillation in the density ratio $\frac{\rho_h}{\rho_l} = 100$ at (a) $t = 0$, (b) $t = 1700$, (c) $t = 2700$, and (d) $t = 4000$. Model A is shown with a black line and model B is shown with a red dashed line. Lines are on top of each other.

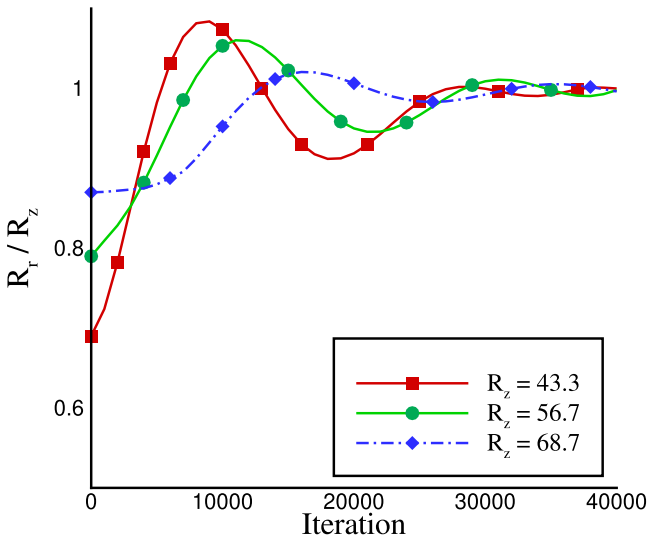

FIG. 15. Time evolution of the half-axis length R_r at different density ratios.

The numerical prediction of droplet oscillation frequency with corresponding analytical results are shown in Table XIII for different R_e. The simulation results are compared to the analytical solution and results presented by Liang *et al.* [31]. It can be seen that the computed frequency has a good agreement with the semianalytical solution and the maximum error is 8.4%. The calculated frequencies for our simulation are very close to those from Liang *et al.* [31].

The influence of the density ratio on the oscillating frequency is investigated. We use the present model to simulate this case with three different densities, $\frac{\rho_h}{\rho_l} = 10, 50, 100$, and the droplet size is set to $R_r = 30, R_z = 90$. The numerical predictions of the oscillating frequency obtained from the present LB model with various density ratios are summarized in Table XIV together with the corresponding analytical results and Liang [31] LB model. It can be seen that increasing density ratio decreases the droplet oscillating frequency, and the computed oscillating frequencies show good agreement with the analytical results as well as Liang's model [31] for all density ratios, with a maximum error of about 9.0%.

V. CONCLUSION

In this work, a comparative study on two state-of-the-art LB phase-field models based on the CACE is performed to evaluate the accuracy of these models to track interfaces. It has been shown that the recovered equation for model A (the Geier model [14]) has additional terms that emerge from the expansion. Meanwhile, model B (the Wang [16] and Ren [15] models) can recover the CACE exactly; however, this comes at the expense of having an additional temporal term in the source term of the LB equation that is undesirable from the perspective of high-performance computing or adaptive mesh refinement. Two regimes of Pe number are used to explain why the additional terms in model A are negligible. When the Pe number is small, the Ma number should be small due to limitations of values that mobility and interface thickness can take. As a consequence, the additional terms are negligible because of a second-order relationship with the Ma number. For large Pe number, the additional terms cancel each other out due to a scaling with $\frac{1}{\mathrm{Pe}}$. Then, we demonstrated, through a series of tests under varying Pe numbers, that the effects of the additional terms are indeed negligible. Both models are very comparable in terms of accuracy in interface tracking.

Additionally, we showed that the two models in their axisymmetric form produce almost the same results which again confirm that the additional terms appear in the recovered interface-tracking equation of model A can be ignored. It was shown that the phase-field interface tracking model cannot conserve mass. We conducted an analysis to show that violation of mass conservation is inherent in these phase-field equations.

Overall, the two LB models that are the focus of this study are roughly comparable in terms of tracking interfaces in the Cartesian and axisymmetric coordinates. Model B is very slightly more accurate, but we argue that model A also has benefits over model B that, depending on the application and interest, can outweigh this gain as it is more amenable to high-performance computing and nonuniform grids processes (e.g., Ref. [35]).

TABLE XIII. Comparison between oscillation frequency for models A and B to the analytical solution $\frac{\rho_h}{\rho_l} = 100$.

R_e	43.3	56.7	68.7
$10^4\omega_{\mathrm{LBA}}$	4.9823	3.3929	2.5161
$10^4\omega_{\mathrm{Liang}}$ [31]	4.9822	3.3929	2.5161
$10^4\omega_{\mathrm{ana}}$	5.3764	3.5864	2.6908
$E_{r_A} = \frac{\lvert\omega_{\mathrm{LB}_A} - \omega_{\mathrm{ana}}\rvert}{\omega_{\mathrm{ana}}} \times 100$	8.4	4.99	6.49
$E_{r_{\mathrm{Liang}}} = \frac{\lvert\omega_{\mathrm{Liang}} - \omega_{\mathrm{ana}}\rvert}{\omega_{\mathrm{ana}}} \times 100$	8.4	4.99	6.49

TABLE XIV. Comparison between the computed oscillating frequency ω_{LB_A} with Liang [31] and analytical solution at different density ratios.

$\frac{\rho_h}{\rho_l}$	10	50	100
$10^4\omega_{\mathrm{LBA}}$	15.2511	7.0428	4.8931
$10^4\omega_{\mathrm{Liang}}$ [31]	15.2504	7.0439	4.8923
$10^4\omega_{\mathrm{ana}}$	16.5854	7.5895	5.3764
$E_{r_A} = \frac{\lvert\omega_{\mathrm{LB}_A} - \omega_{\mathrm{ana}}\rvert}{\omega_{\mathrm{ana}}} \times 100$	8.0	7.2	9.0
$E_{r_{\mathrm{Liang}}} = \frac{\lvert\omega_{\mathrm{LB}_{\mathrm{Liang}}} - \omega_{\mathrm{ana}}\rvert}{\omega_{\mathrm{ana}}} \times 100$	8.0	7.2	8.9

ACKNOWLEDGMENT

We acknowledge and are grateful for funding by the National Science Foundation under Award No. CBET-1803989.

APPENDIX A: MODEL A LBE

The evolution equation of the LB model for model A is written as

$$h_i(\boldsymbol{x} + \boldsymbol{c}_i\delta t, t + \delta t) - h_i(\boldsymbol{x}, t) = -\frac{h_i(\boldsymbol{x}, t) - h_{i,A}^{\mathrm{eq}}(\boldsymbol{x}, t)}{\tau} + \left(1 - \frac{1}{2\tau}\right)\delta t F_{i,A}(\boldsymbol{x}, t). \quad \text{(A1)}$$

The following equations are the constraints of $h_{i,A}^{\mathrm{eq}}$ and $F_{i,A}$ for model A:

$$\sum_i h_{i,A}^{\mathrm{eq}} = \phi, \tag{A2}$$

$$\sum_i \boldsymbol{c}_i h_{i,A}^{\mathrm{eq}} = \phi \boldsymbol{u}, \tag{A3}$$

$$\sum_i \boldsymbol{c}_i \boldsymbol{c}_i h_{i,A}^{\mathrm{eq}} = c_s^2 \phi \mathbf{I} + \phi \boldsymbol{u}\boldsymbol{u}, \tag{A4}$$

$$\sum_i F_{i,A} = 0, \tag{A5}$$

$$\sum_i \boldsymbol{c}_i F_{i,A} = c_s^2 \frac{\boldsymbol{\nabla}\phi}{|\boldsymbol{\nabla}\phi|}\lambda, \tag{A6}$$

$$\sum_i \boldsymbol{c}_i \boldsymbol{c}_i F_{i,A} = 0. \tag{A7}$$

The multiscaling expansion of the distribution function, time derivative, space gradient, and discrete source term are introduced such that

$$h_i = h_i^{(0)} + \epsilon h_i^{(1)} + \epsilon^2 h_i^{(2)} + \dots, \tag{A8}$$

$$\partial_t = \epsilon \partial_{i_1} + \epsilon^2 \partial_{i_2}, \tag{A9}$$

$$\boldsymbol{\nabla} = \epsilon \boldsymbol{\nabla}_{\mathbf{1}}, \tag{A10}$$

and

$$F_{i,A} = \epsilon F_i^{(1)} + \epsilon^2 F_i^{(2)}, \tag{A11}$$

where ϵ is a small expansion parameter. By Taylor expanding Eq. (A1),

$$D_i h_i + \frac{\delta t}{2} D_i^2 h_i + \dots = -\frac{1}{\tau \delta t}\left(h_i - h_i^{\mathrm{eq}}\right) + \left(1 - \frac{1}{2\tau}\right) F_{i,A}, \tag{A12}$$

where $D_i = \partial_t + \boldsymbol{c}_i \cdot \boldsymbol{\nabla}$. Substituting Eqs. (A8)–(A11) into Eq. (A12), one gets

$$\begin{aligned}
&\left(\epsilon \partial_{i_1} + \epsilon^2 \partial_{i_2} + \epsilon \boldsymbol{\nabla}_{\mathbf{1}}\right)\left[h_i^{(0)} + \epsilon h_i^{(1)} + \epsilon^2 h_i^{(2)} + \dots\right] \\
&\quad + \frac{\delta t}{2}\left(\epsilon \partial_{i_1} + \epsilon^2 \partial_{i_2} + \epsilon \boldsymbol{\nabla}_{\mathbf{1}}\right)\left[h_i^{(0)} + \epsilon h_i^{(1)} + \epsilon^2 h_i^{(2)} + \dots\right] \\
&= -\frac{1}{\tau \delta t}\left[h_i^{(0)} + \epsilon h_i^{(1)} + \epsilon^2 h_i^{(2)} + \dots - h^{\mathrm{eq}}\right] \\
&\quad + \epsilon\left(1 - \frac{1}{2\tau}\right) F_i^{(1)} + \epsilon^2 \left(1 - \frac{1}{2\tau}\right) F_i^{(2)}.
\end{aligned} \tag{A13}$$

Thus, the zeroth-, first-, and second-order equations in parameter ϵ can be written as

$$\epsilon^0 : h_i^{(0)} = h_i^{\mathrm{eq}}, \tag{A14}$$

$$\epsilon^1 : (\partial_{t_1} + \boldsymbol{c}_i \cdot \boldsymbol{\nabla}_{\mathbf{1}}) h_i^{(0)} = -\frac{1}{\tau \delta t} h_i^{(1)} + \left(1 - \frac{1}{2\tau}\right) F_i^{(1)}, \tag{A15}$$

$$\begin{aligned}
\epsilon^2 : \partial_{t_2} h_i^{(0)} + (\partial_{t_1} + \boldsymbol{c}_i \cdot \boldsymbol{\nabla}_{\mathbf{1}}) h_i^{(1)} + \frac{\delta t}{2}(\partial_{t_1} + \boldsymbol{c}_i \cdot \boldsymbol{\nabla}_{\mathbf{1}})^2 h_i^{(0)} \\
= -\frac{1}{\tau \delta t} h_i^{(2)} + \left(1 - \frac{1}{2\tau}\right) F_i^{(2)},
\end{aligned} \tag{A16}$$

Multiplying Eq. (A15) to $\frac{\delta t}{2}(\partial_{t_1} + c_i \cdot \boldsymbol{\nabla}_{\mathbf{1}})$, one can obtain

$$\frac{\delta t}{2}(\partial_{t_1} + \boldsymbol{c}_i \cdot \boldsymbol{\nabla}_{\mathbf{1}})^2 h_i^{(0)} = -\frac{1}{2\tau}(\partial_{t_1} + \boldsymbol{c}_i \cdot \boldsymbol{\nabla}_{\mathbf{1}}) h_i^{(1)} + \frac{\delta t}{2}(\partial_{t_1} + \boldsymbol{c}_i \cdot \boldsymbol{\nabla}_{\mathbf{1}})\left(1 - \frac{1}{2\tau}\right) F_i^{(1)}. \tag{A17}$$

Substituting Eq. (A17) into Eq. (A16), we can rewrite it as

$$\epsilon^2 : \partial_{t_2} h_i^{(0)} + \left(1 - \frac{1}{2\tau}\right)(\partial_{t_1} + \boldsymbol{c}_i \cdot \boldsymbol{\nabla}_{\mathbf{1}}) h_i^{(1)} + \left(1 - \frac{1}{2\tau}\right)\frac{\delta t}{2}(\partial_{t_1} + \boldsymbol{c}_i \cdot \boldsymbol{\nabla}_{\mathbf{1}}) F_i^{(1)} = -\frac{1}{\tau \delta t} h_i^{(2)} + \left(1 - \frac{1}{2\tau}\right) F_i^{(2)}, \tag{A18}$$

The recovered equations at scale ϵ^1 and ϵ^2 can be obtained by summation of Eq. (A15) and Eq. (A18) over i, respectively,

$$\partial_{t_1} \phi + \boldsymbol{\nabla}_1 \cdot (\phi \boldsymbol{u}) = 0, \tag{A19}$$

$$\partial_{t_2} \phi + \left(1 - \frac{1}{2\tau}\right)\left[\boldsymbol{\nabla}_{\mathbf{1}} \cdot \sum_i \boldsymbol{c}_i h_i^{(1)}\right] + \left(1 - \frac{1}{2\tau}\right)\frac{\delta t}{2} c_s^2 \left[\partial_{t_1}(\phi \boldsymbol{u}) + \frac{\boldsymbol{\nabla}_{\mathbf{1}}\phi}{|\boldsymbol{\nabla}_{\mathbf{1}}\phi|}\lambda\right] = 0. \tag{A20}$$

By multiplying Eq. (A15) with c_i and summing over i, one can get

$$\sum_i c_i h_i^{(1)} = (-\tau \delta t)\left[\partial_{t_1}(\phi \boldsymbol{u}) + \boldsymbol{\nabla}_{\mathbf{1}}\left(c_s^2 \phi \mathbf{I} + \phi \boldsymbol{u}\boldsymbol{u}\right) - \left(1 - \frac{1}{2\tau}\right)\left(c_s^2 \frac{\boldsymbol{\nabla}_{\mathbf{1}}\phi}{|\boldsymbol{\nabla}_{\mathbf{1}}\phi|}\lambda\right)\right], \tag{A21}$$

where $M = c_s^2(\tau - \frac{1}{2})\delta_t$ is the mobility. Substitution of Eq. (A21) into (A20) leads to

$$\partial_{t_2}\phi - \left\{\boldsymbol{\nabla}_{\mathbf{1}} \cdot \left[M\left(\boldsymbol{\nabla}_{\mathbf{1}}\phi - \lambda \frac{\boldsymbol{\nabla}_{\mathbf{1}}\phi}{|\boldsymbol{\nabla}_{\mathbf{1}}\phi|}\right)\right] + \boldsymbol{\nabla}_{\mathbf{1}}[\partial t_1(\phi \boldsymbol{u})]\frac{M}{c_s^2} + \boldsymbol{\nabla}_{\mathbf{1}}^2(\phi \boldsymbol{u}\boldsymbol{u})\frac{M}{c_s^2}\right\} = 0. \tag{A22}$$

Combining Eqs. (A19) and (A22) at t_1 and t_2, we can have

$$\frac{\partial \phi}{\partial t} + \boldsymbol{\nabla} \cdot (\phi \boldsymbol{u}) = \boldsymbol{\nabla} \cdot \left[M\left(\boldsymbol{\nabla}\phi - \lambda \boldsymbol{n}\right)\right] + \boldsymbol{\nabla}\left[\frac{\partial(\phi \boldsymbol{u})}{\partial t}\right]\frac{M}{c_s^2} + \boldsymbol{\nabla}^2(\phi \boldsymbol{u}\boldsymbol{u})\frac{M}{c_s^2}, \tag{A23}$$

which shows the A-C equation associated to model A.

APPENDIX B: AXISYMMETRIC LB MODEL A

Macroscopic values for the axisymmetric form of model A are

$$\sum_i h_{i,A}^{\mathrm{eq}} = r\phi, \tag{B1}$$

$$\sum_i c_{i\alpha} h_{i,A}^{\mathrm{eq}} = r\phi u_\alpha + M\phi\delta_{\alpha r}, \tag{B2}$$

$$\sum_i c_{i\alpha} c_{i\alpha} h_{i,A}^{\mathrm{eq}} = c_s^2 r\phi + r\phi u_\alpha u_\alpha, \tag{B3}$$

$$\sum_i F_{i,A} = 0, \tag{B4}$$

$$\sum_i c_{i\alpha} F_{i,A} = c_s^2 n_\alpha \lambda, \tag{B5}$$

$$\sum_i c_{i\alpha} c_{i\alpha} F_{i,A} = 0, \tag{B6}$$

Substituting Eqs. (B1)–(B6) into Eqs. (23) and (24) and summing over i leads to

$$\partial_{t_1}(r\phi) + \partial_\alpha(r\phi u_\alpha + M\phi\delta_{\alpha r}) = 0, \tag{B7}$$

$$\partial_{t_2}(r\phi) + (1 - \frac{1}{2\tau})(\partial_\alpha . \sum_i c_{i\alpha} h_i^1) + \left(1 - \frac{1}{2\tau}\right)\frac{\delta t}{2} \times c_s^2[\partial_{t_1}(r\phi u_\alpha + r\phi u_\alpha u_\alpha + M\phi\delta_{\alpha r}) + r n_\alpha \lambda] = 0. \tag{B8}$$

By manipulating Eq. (B8), we can rewrite in the following form:

$$\partial_{t_2}(r\phi) - \partial_\alpha M[\partial_\alpha(r\phi) - r n_\alpha \lambda] - \partial_\alpha \partial_{t_1}(r\phi u_\alpha) - \partial_\alpha(\partial_\alpha r\phi u_\alpha u_\alpha) - M c_s^2 \partial_\alpha\left[\partial_{t_1}(M\phi\delta_{\alpha r})\right] = 0. \tag{B9}$$

Summation of (B7) and (B9) leads to axisymmetric form of conservative A-C equation,

$$\partial_t(r\phi) + \partial_\alpha(r\phi u_\alpha + M\phi\delta_{\alpha r}) = \partial_\alpha M(\partial_\alpha(r\phi) - r n_\alpha\lambda) + \frac{M}{c_s^2}\partial_\alpha\partial_{t_1}(r\phi u_\alpha) + \frac{M}{c_s^2}\partial_\alpha(\partial_\alpha r\phi u_\alpha u_\alpha) + \frac{M}{c_s^2}\partial_\alpha[\partial_{t_1}(M\phi\delta_{\alpha r})]. \tag{B10}$$

APPENDIX C: ADDITIONAL TERM

Part 2 of the error terms can be written as:

$$\frac{M}{c_s^2}\nabla\cdot\left[\phi\left(\frac{\partial \boldsymbol{u}}{\partial t} + \boldsymbol{u}.\nabla\boldsymbol{u}\right)\right]. \tag{C1}$$

The N-S equation for in-compressible two-phase flows is as follows:

$$\frac{\partial \boldsymbol{u}}{\partial t} + \boldsymbol{u}\cdot\nabla\boldsymbol{u} = -\frac{\nabla p}{\rho} + \mu_\phi\nabla\phi + \nu\nabla^2\boldsymbol{u}. \tag{C2}$$

Dimensionless form of Eq. (C2) express as:

$$\frac{\partial \boldsymbol{u}^*}{\partial t} + \boldsymbol{u}^*.\nabla^*\boldsymbol{u}^* = -\nabla^* p^* + \frac{\mu_\phi}{U^2}\mu_\phi\nabla^*\phi + \frac{1}{\mathrm{Re}}\nabla^{*2}\boldsymbol{u}^*. \tag{C3}$$

Thus, dimensionless form of part 2 of error terms is

$$\frac{MU^2}{c_s^2 L^2}\nabla^*\cdot\left[\phi\left(\frac{\partial \boldsymbol{u}^*}{\partial t} + \boldsymbol{u}^*.\nabla^*\boldsymbol{u}^*\right)\right]. \tag{C4}$$

Plugging Eq. (C2) into Eq. (C4) and dividing by U/L leads to:

$$\frac{\mathrm{Ma}^2}{\mathrm{Pe}}\nabla^*\cdot\left[\phi\left(-\nabla^* p^* + \frac{\mu_\phi}{U^2}\nabla^*\phi + \frac{1}{\mathrm{Re}}\nabla^{*2}\boldsymbol{u}^*\right)\right]. \tag{C5}$$

As we know, this LB model is applicable for the Ma < 0.3 [35]. Two regimes of Mach number are defined to analyze this term. In the first regime (Ma $\ll 0.3$), this dimensionless number ($\frac{\mathrm{Ma}^2}{\mathrm{Pe}} \ll 1$) is very small. As a result, the error terms are negligible. In the second regime [Ma $\sim O(0.3)$], this dimensionless number ($\frac{\mathrm{Ma}^2}{\mathrm{Pe}}$) is at least one order of magnitude larger than the first regime. In order to evaluate the error term in a relatively large Mach number [Ma $\sim O(0.3)$], each of the error terms in Eq. (C5) is considered separately. First, viscous stress term has a relationship with ($\frac{1}{\mathrm{Re}}$). For the larger velocity, the Reynolds number is relatively large Re > 10 and [$\frac{\mathrm{Ma}^2}{\mathrm{Pe}}\nabla^*(\frac{1}{\mathrm{Re}}\nabla^{*2}\boldsymbol{u}^*)$] is negligible. Second, the surface tension force is related to the chemical potential. This chemical potential (μ_ϕ) is always $\mu_\phi \ll 1$ and multiplying this term into the ($\frac{\mathrm{Ma}^2}{\mathrm{Pe}}$), which is a small term, leads to the negligible term. Third, the hydrodynamic pressure ($\frac{\mathrm{Ma}^2}{\mathrm{Pe}}\nabla^* p^*$). For the relatively high velocity, the pressure term is degrading due to incompressible condition. Multiplying second-order pressure gradient to this parameter ($\frac{\mathrm{Ma}^2}{\mathrm{Pe}} \ll 1$) is also making this term much smaller. Therefore, this term can be neglected.

[1] S. O. Unverdi and G. Tryggvason, A front-tracking method for viscous, incompressible, multi-fluid flows, J. Comput. Phys. **100**, 25 (1992).

[2] M. Sussman, P. Smereka, and S. Osher, A level set approach for computing solutions to incompressible two-phase flow, J. Comput. Phys. **114**, 146 (1994).

[3] D. M. Anderson, G. B. McFadden, and A. A. Wheeler, Diffuse-interface methods in fluid mechanics, Annu. Rev. Fluid Mech. **30**, 139 (1998).

[4] D. Jacqmin, Calculation of two-phase Navier–Stokes flows using phase-field modeling, J. Comput. Phys. **155**, 96 (1999).

[5] J. W. Cahn and J. E. Hilliard, Free energy of a nonuniform system. i. Interfacial free energy, J. Chem. Phys. **28**, 258 (1958).

[6] S. M. Allen and J. W. Cahn, Mechanisms of phase transformations within the miscibility gap of fe-rich fe-al alloys, Acta Metall. **24**, 425 (1976).

[7] A. Fakhari and M. H. Rahimian, Phase-field modeling by the method of lattice Boltzmann equations, Phys. Rev. E **81**, 036707 (2010).

[8] T. Lee and L. Liu, Lattice boltzmann simulations of micron-scale drop impact on dry surfaces, J. Comput. Phys. **229**, 8045 (2010).

[9] Y. Zu and S. He, Phase-field-based lattice Boltzmann model for incompressible binary fluid systems with density and viscosity contrasts, Phys. Rev. E **87**, 043301 (2013).

[10] H. Liang, B. Shi, Z. Guo, and Z. Chai, Phase-field-based multiple-relaxation-time lattice Boltzmann model for incompressible multiphase flows, Phys. Rev. E **89**, 053320 (2014).

[11] P. Yue, C. Zhou, and J. J. Feng, Spontaneous shrinkage of drops and mass conservation in phase-field simulations, J. Comput. Phys. **223**, 1 (2007).

[12] Y. Sun and C. Beckermann, Sharp interface tracking using the phase-field equation, J. Comput. Phys. **220**, 626 (2007).

[13] P.-H. Chiu and Y.-T. Lin, A conservative phase field method for solving incompressible two-phase flows, J. Comput. Phys. **230**, 185 (2011).

[14] M. Geier, A. Fakhari, and T. Lee, Conservative phase-field lattice Boltzmann model for interface tracking equation, Phys. Rev. E **91**, 063309 (2015).

[15] F. Ren, B. Song, M. C. Sukop, and H. Hu, Improved lattice Boltzmann modeling of binary flow based on the conservative Allen-Cahn equation, Phys. Rev. E **94**, 023311 (2016).

[16] H. Wang, Z. Chai, B. Shi, and H. Liang, Comparative study of the lattice Boltzmann models for Allen-Cahn and Cahn-Hilliard equations, Phys. Rev. E **94**, 033304 (2016).

[17] H. Liang, J. Xu, J. Chen, H. Wang, Z. Chai, and B. Shi, Phase-field-based lattice Boltzmann modeling of large-density-ratio two-phase flows, Phys. Rev. E **97**, 033309 (2018).

[18] H. Wang, X. Yuan, H. Liang, Z. Chai, and B. Shi, A brief review of the phase-field-based lattice Boltzmann method for multiphase flows, Capillarity **2**, 33 (2019).

[19] D. Link, S. L. Anna, D. Weitz, and H. A. Stone, Geometrically Mediated Breakup of Drops in Microfluidic Devices, Phys. Rev. Lett. **92**, 054503 (2004).

[20] A. S. Utada, A. Fernandez-Nieves, H. A. Stone, and D. A. Weitz, Dripping to Jetting Transitions in Coflowing Liquid Streams, Phys. Rev. Lett. **99**, 094502 (2007).

[21] J. Hua and J. Lou, Numerical simulation of bubble rising in viscous liquid, J. Comput. Phys. **222**, 769 (2007).

[22] H. Huang, J.-J. Huang, and X.-Y. Lu, A mass-conserving axisymmetric multiphase lattice Boltzmann method and its application in simulation of bubble rising, J. Comput. Phys. **269**, 386 (2014).

[23] A. Begmohammadi, M. Farhadzadeh, and M. H. Rahimian, Simulation of pool boiling and periodic bubble release at high density ratio using lattice Boltzmann method, Int. Commun. Heat Mass Transfer **61**, 78 (2015).

[24] A. Begmohammadi, M. Rahimian, M. Farhadzadeh, and M. A. Hatani, Numerical simulation of single-and multi-mode film boiling using lattice Boltzmann method, Comput. Math. Appl. **71**, 1861 (2016).

[25] M. A. Hatani, H. Amirshaghaghi, M. Rahimian, and A. Begmohammadi, Lattice Boltzmann simulation of condensation over different cross sections and tube banks, J. Mech. Sci. Techn. **31**, 4943 (2017).

[26] J. G. Zhou, Axisymmetric lattice Boltzmann method revised, Phys. Rev. E **84**, 036704 (2011).

[27] K. N. Premnath and J. Abraham, Lattice Boltzmann model for axisymmetric multiphase flows, Phys. Rev. E **71**, 056706 (2005).

[28] X. He, S. Chen, and R. Zhang, A lattice Boltzmann scheme for incompressible multiphase flow and its application in simulation of rayleigh–taylor instability, J. Comput. Phys. **152**, 642 (1999).

[29] S. Mukherjee and J. Abraham, Lattice Boltzmann simulations of two-phase flow with high density ratio in axially symmetric geometry, Phys. Rev. E **75**, 026701 (2007).

[30] H. Liang, Z. H. Chai, B. C. Shi, Z. L. Guo, and T. Zhang, Phase-field-based lattice Boltzmann model for axisymmetric multiphase flows, Phys. Rev. E **90**, 063311 (2014).

[31] H. Liang, Y. Li, J. Chen, and J. Xu, Axisymmetric lattice Boltzmann model for multiphase flows with large density ratio, Int. J. Heat Mass Transf. **130**, 1189 (2019).

[32] A. Fakhari, T. Mitchell, C. Leonardi, and D. Bolster, Improved locality of the phase-field lattice-Boltzmann model for immiscible fluids at high density ratios, Phys. Rev. E **96**, 053301 (2017).

[33] X. He and L.-S. Luo, *A priori* derivation of the lattice Boltzmann equation, Phys. Rev. E **55**, R6333 (1997).

[34] A. Fakhari, Y. Li, D. Bolster, and K. T. Christensen, A phase-field lattice Boltzmann model for simulating multiphase flows in porous media: Application and comparison to experiments of co2 sequestration at pore scale, Adv. Water Resour. **114**, 119 (2018).

[35] A. Fakhari, D. Bolster, and L.-S. Luo, A weighted multiple-relaxation-time lattice Boltzmann method for multiphase flows and its application to partial coalescence cascades, J. Comput. Phys. **341**, 22 (2017).

[36] A. Fakhari and D. Bolster, Diffuse interface modeling of three-phase contact line dynamics on curved boundaries: A lattice Boltzmann model for large density and viscosity ratios, J. Comput. Phys. **334**, 620 (2017).

[37] R. Haghani-Hassan-Abadi and M.-H. Rahimian, Axisymmetric lattice Boltzmann model for simulation of ternary fluid flows, Acta Mech. **231**, 2323 (2020).

[38] S. T. Zalesak, Fully multidimensional flux-corrected transport algorithms for fluids, J. Comput. Phys. **31**, 335 (1979).

[39] R. Haghani-Hassan-Abadi, A. Fakhari, and M.-H. Rahimian, Numerical simulation of three-component multiphase flows at high density and viscosity ratios using lattice Boltzmann methods, Phys. Rev. E **97**, 033312 (2018).

[40] R. Haghani-Hassan-Abadi, M.-H. Rahimian, and A. Fakhari, Conservative phase-field lattice-Boltzmann model for ternary fluids, J. Comput. Phys. **374**, 668 (2018).

[41] D. Bhaga and M. Weber, Bubbles in viscous liquids: Shapes, wakes and velocities, J. Fluid Mech. **105**, 61 (1981).

[42] R. F. Mudde, Gravity-driven bubbly flows, Annu. Rev. Fluid Mech. **37**, 393 (2005).

[43] S. Srivastava, P. Perlekar, J. H. ten Thije Boonkkamp, N. Verma, and F. Toschi, Axisymmetric multiphase lattice Boltzmann method, Phys. Rev. E **88**, 013309 (2013).

[44] H. Liu, L. Wu, Y. Ba, G. Xi, and Y. Zhang, A lattice Boltzmann method for axisymmetric multicomponent flows with high viscosity ratio, J. Comput. Phys. **327**, 873 (2016).

[45] C. Miller and L. Scriven, The oscillations of a fluid droplet immersed in another fluid, J. Fluid Mech. **32**, 417 (1968).